



Available online at www.sciencedirect.com

ScienceDirect

Comput. Methods Appl. Mech. Engrg. 410 (2023) 115982

Computer methods in applied mechanics and engineering

www.elsevier.com/locate/cma

A multiscale phase field fracture approach based on the non-affine microsphere model for rubber-like materials

Prajwal Kammardi Arunachala, Sina Abrari Vajari, Matthias Neuner, Christian Linder*

Department of Civil and Environmental Engineering, Stanford University, Stanford, CA, 94305, USA

Received 1 January 2023; accepted 27 February 2023 Available online 27 March 2023

Abstract

Rubber-like materials have a broad scope of applications due to their unique properties like high stretchability and increased toughness. Hence, computational models for simulating their fracture behavior are paramount for designing them against failures. In this study, the phase field fracture approach is integrated with a multiscale polymer model for predicting the fracture behavior in elastomers. At the microscale, damaged polymer chains are modeled to be made up of a number of elastic chain segments pinned together. Using the phase field approach, the damage in the chains is represented using a continuous variable. Both the bond stretch internal energy and the entropic free energy of the chain are assumed to drive the damage, and the advantages of this assumption are expounded. A framework for utilizing the non-affine microsphere model for damaged systems is proposed by considering the minimization of a hypothetical undamaged free energy, ultimately connecting the chain stretch to the macroscale deformation gradient. At the macroscale, a thermodynamically consistent formulation is derived in which the total dissipation is assumed to be mainly due to the rupture of molecular bonds. Using a monolithic scheme, the proposed model is numerically implemented and the resulting three-dimensional simulation predictions are compared with existing experimental data. The capability of the model to qualitatively predict the propagation of complex crack paths and quantitatively estimate the overall fracture behavior is verified. Additionally, the effect of the length scale parameter on the predicted fracture behavior is studied for an inhomogeneous system.

Keywords: Phase field fracture approach; Non-affine microsphere model; Multiscale model; Fracture propagation; Rubber-like materials

1. Introduction

Rubber-like materials are known for their desirable properties like high stretchability, low stiffness, and high toughness, and hence find myriad applications in many blooming fields like stretchable electronics. Additionally, the possibility of their combination with carbon nanotubes or conjugated polymers to create stretchable conductors or semiconductors makes them a perfect choice for future applications in devices like self-actuators, epidermal electronics, and implantable sensors [1,2]. Elastomers also find many biological applications in fields like soft robotics [3,4], tissue engineering [5,6], and biomedical implants [7]. Due to their low cost and low weight, rubberbased materials have a wide range of industrial applications like tires, seals, hoses, and airbags [8–10]. Therefore,

E-mail address: linder@stanford.edu (C. Linder).

^{*} Corresponding author.

computational models for simulating the fracture behavior of rubber-like materials are vital for quantifying their behavior and designing against fracture or fatigue failures.

Early studies in this field often used classical fracture mechanics to present failure criteria for estimating the crack initiation and the ultimate fracture behavior of rubber-like materials. One of the earliest investigations was performed by Rivlin and Thomas [11], wherein a critical macroscopic fracture toughness or tearing energy of rubbers was defined in line with the critical energy release rate proposed by Griffith [12] in order to predict the incipient and catastrophic tearing of rubber specimens. Pidaparti et al. [13] applied this concept for predicting the critical loads in specimens subjected to mixed mode loading. Further extending this concept, Hocine et al. [14,15] and Hocine and Abdelaziz [16] studied the evaluation of the fracture toughness of rubber as the critical value of J-integral at crack initiation in a notched specimen. In other works, Kawabata [17] proposed a fracture criterion based on a critical stretch for rubber-like materials under biaxial stress states, and Hamdi et al. [18] extended this for different biaxiality loading ratios. Even recently, failure criteria based on critical local energy release rate for fatigue fracture [19], local strain energy density for cracked and V-notched specimens [20], and critical effective stretch for mode-I crack loading [21], have been proposed for these elastomers. However, these methods have been found to exhibit mesh dependency during numerical simulations, require additional crack propagation criteria and become inapplicable for modeling complex multi-crack interactions [22]. This necessitates using continuum damage models to simulate the crack propagation in rubber-like materials.

In order to overcome the above limitations, phase field method has been commonly used for modeling the crack propagation in such materials. This continuum approach represents discontinuities in a diffusive manner and involves a length scale for gradient effects of damage. In the mechanics community, the study by Francfort and Marigo [23] was the pioneering work that proposed a variational formulation for brittle fracture using the phase field idea. This method was regularized by Bourdin et al. [24] using a length scale, thus making it suitable for numerical simulations. One of the first works to develop a framework in the finite deformation setting for utilization of the phase field method for modeling fracture in rubbery polymers was by Miehe and Schänzel [25]. Since then, the phase field method has been used in many large deformation applications like anisotropic biological tissues [26,27], fiber-reinforced composite laminates [28,29], thermo-elastic-plastic solids [30], ductile fracture [31,32] and hydrogels [33,34].

For rubber-like materials, many researchers have extended the framework proposed by Miehe and Schänzel [25] and have developed models using the macroscale critical energy release rate, in line with Griffith's theory. Wu et al. [35] applied the phase field method to study rupture in carbon black reinforced natural rubber composites and performed a Monte Carlo simulation to quantify the uncertainty in their failures. A phase-transition theory was proposed by Kumar et al. [36] for modeling the crack propagation and healing in elastomers by assuming the fracture nucleation to occur in regions of large stress concentrations. For capturing the rate-dependent behavior of rubbers, Loew et al. [8] accounted for their viscosity in the description of the bulk as well as in the damage driving force. Improving on this, Yin and Kaliske [37] proposed a phase field method coupled with a viscoelastic rheological approach for general viscoelastic polymers while considering only the elastic stored energy to drive the damage. The phase field method was extended for modeling high-speed crack instability in general hyperelastic materials by Tian et al. [38] by deriving a dynamic model based on the non-conservative Lagrange equation. The competition between the damage in the bulk and interfaces in bilayer composites made of rubber-like materials was studied by Marulli et al. [39] by integrating with the cohesive zone approach to model the imperfect interfaces. A higher-order phase field theory for hyperelastic rubbers was proposed by Peng et al. [40] for improving the numerical efficiency. Many recent researchers have incorporated the incompressible nature of rubbers in their phase field approaches and have proposed stabilized formulations [41-44]. The aforementioned phase field approaches combined with macroscale elastomer models are based on Griffith's theory. Although this has been found to hold for specimens with macroscopic flaws, Chen et al. [45] used experiments to demonstrate that Griffith's theory's fundamental flaw-sensitive behavior assumption fails at very small length scales, which can range from nanometers to centimeters depending on the material. Further, it is advantageous to account for the micro-mechanical behavior of the polymers for coupling the effects of complex microscale phenomena like strain-induced crystallization [46]. This motivates the need for developing multiscale models and coupling them with the phase field theory for generalized utility.

A key component of an effective multiscale theory is a network model that bridges the deformations at the two scales. Early network theories like the three-chain model [47,48] assumed the deformation mapping of the

chains along the principal stretch directions to be the same as that at the macroscale, which is referred to as affine deformation. As this was observed to over-constrain the system, the concept of non-affine deformation was introduced by allowing chain reorientations to redistribute the stress more flexibly and attain lower energy states while simultaneously satisfying kinematic compatibility. The most commonly used eight-chain model [49] considers an effective non-affine response of the overall network by assuming affine deformation of the representative chains oriented along the diagonals of a unit cubic cell. However, this model has been found to exhibit a fixed relationship between locking stretches for different deformation modes [50,51], and hence is inefficient in simultaneously estimating different multi-axial responses [52]. To overcome this limitation, the microsphere model proposed by Miehe et al. [50] introduces non-affinity with the help of a fluctuation field, which is solved utilizing the principle of averaged free energy subjected to a *p*-root average constraint. Additionally, the restricted movement of a single polymer chain using a tube-like constraint is considered in order to account for the effects of crosslinks and entanglements. The effectiveness of this non-affine model in capturing inelastic effects in rubbers like viscoelasticity [53,54], anisotropic Mullins-type damage [55] and strain-induced crystallization [56] has been studied in the literature. Due to its capability, the non-affine microsphere model can be well suited for accurately capturing the damaged response of rubber-like materials which are subjected to complex loadings.

Among the fracture studies that incorporate microscale properties, one of the earliest attempts was done by Lake and Thomas [57], wherein the critical energy release rate of rubbers was expressed in terms of the binding energy between the monomer units. Recognizing its importance, Mao et al. [58] incorporated the internal energy due to molecular bond stretching by assuming the chain segments to be elastic and proposed a fracture criterion based on the critical bond rupture energy. Building on this theory, Talamini et al. [59] utilized the eight-chain model and developed a novel phase field model for elastomers by assuming fracture to be solely propelled by the internal molecular distortional energy. Li and Bouklas [60] also used the eight-chain network model and simulated the fracture in nearly-incompressible polydisperse elastomer networks by using a critical energy release rate obtained with the help of the critical bond dissociation energy. Micromechanically motivated constitutive models, wherein the effective macroscale damage is obtained by homogenization of the anisotropic microscale chain damage, were developed and tested for uniaxial tension case by Mulderrig et al. [61]. The aforementioned study investigates the efficacy of microsphere-based affine and non-affine models bridging the deformations at the two scales. Utilizing the maximal advance path constraint network model [62], the effect of strain-induced crystallization on delaying the onset of fracture initiation in certain rubbers was captured by incorporating bond and crystallite distortional energies into the critical rupture energy by Arunachala et al. [46]. Despite the fact that Swamynathan et al. [63] utilized the phenomenological Gent model of hyperelasticity [64], they considered the dissipation due to bond stretching and validated their phase field approach for multiaxial loading cases of industrially relevant silicone material. Although there is a lack of studies incorporating the non-affine microsphere model proposed by Miehe et al. [50] along with the phase field approach, a few studies utilize it for modeling fracture in elastomers. Dal and Kaliske [51] used it for modeling aging-induced fracture in rubber-like materials, wherein the Morse potential used for the interatomic bond energy captures the failure due to bond rupture. Guo and Zaïri [65] also utilized this non-affine network model for modeling deformation-induced failure in elastomeric media by introducing elastic detachable bonds to account for the time-dependent stochastic chain scission process. However, there is a dearth of studies exploring the effectiveness of the non-affine microsphere network model in estimating fracture behavior for inhomogeneous cases. Furthermore, most of these studies lack in illustrating the applicability of their models for capturing complex crack paths and comparing them with experimental data.

To further the understanding of the fracture behavior and enhance the modeling capacity of the crack propagation in elastomers, we propose a phase field fracture model built on top of a multiscale polymer model, which is bridged using a non-affine network model. At the microscale, the physicality and numerical advantages of considering the entropic energy contribution, in addition to the internal energy due to bond stretch, to the damage driving force is discussed. The non-affine microsphere model is utilized for bridging the deformations at the two scales and a framework for its amalgamation with the damage model is proposed. At the macroscale, a thermodynamically consistent formulation is developed. The bulk energy is assumed to degrade faster than the chain-free energy, and separate damage-driving history variables are introduced. The model is validated by comparing the three-dimensional simulation results with existing experimental data for complex inhomogeneous systems. The effect of the length scale parameter on the predicted load–displacement behavior and crack propagation paths is also investigated.

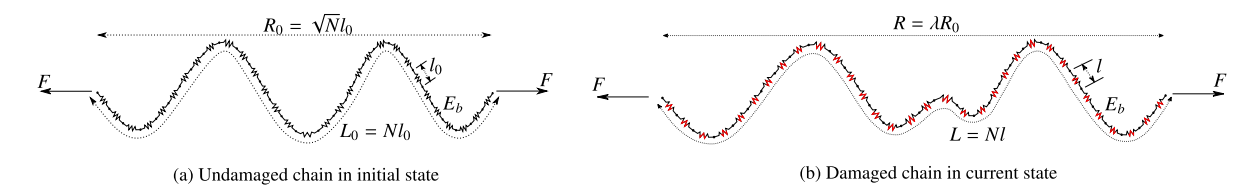


Fig. 1. Models assumed for the undamaged chain in the initial state and a damaged chain in the current state.

The outline of the paper is as follows. The phase field damage approach combined with the multiscale model for elastomers is presented in Section 2. In particular, the microscale damaged chain model is proposed in Section 2.1, a framework for bridging the deformations at the two scales using the non-affine microsphere model is introduced in Section 2.2, and the unified multiscale model with the phase field fracture approach at the macroscale is presented in Section 2.3. The numerical implementation of the model is detailed in Section 3. Numerical simulations are performed and the predictions are validated with existing experimental data in Section 4. Finally, the conclusions are summarized in Section 5, and additional information, derivations, and results are presented in the Appendices.

2. Multiscale fracture model using the phase field approach

The underlying polymer chain network contributes significantly to the unique characteristics of rubber-like materials, which necessitates the microscale modeling for accurately predicting their behavior. Furthermore, accounting for the microscopic molecular bond distortions has been found to be critical for modeling their fracture behavior. On the other hand, the response to external actions can be studied using the macroscale model. The deformations across these two scales can be bridged using network models, which assume kinematic compatibility. A continuum fracture approach can be combined to model the system's damaged response. In this study, the polymer chains at the microscale are modeled to be made up of a number of chain segments. A continuum formulation combined with the phase field fracture approach is utilized to model the damaged macroscale behavior. The deformations in the two scales are connected using the non-affine microsphere model.

It is well-known that viscous dissipation at the crack tip is a contributor to the total energy dissipation at the advancing crack in rubber-like materials [66,67]. However, tearing energies in agreement with the theoretical results of Lake and Thomas [57], which are independent of the crack velocity and ambient temperature, have also been experimentally measured in near-equilibrium conditions [68]. The current study focuses on such cases and neglects viscoelastic effects, similar to many of the previous studies in this field [25,59,60].

2.1. Microscale damaged chain model

Many studies attribute the unique characteristics of rubber-like materials to their underlying polymer chain networks, which makes it vital to model the chain behavior. The classical theories attributed the high stretchability of these materials to the entropy of chain molecules between crosslinks. They modeled them with a series of freely jointed rigid segments having equal lengths. However, the assumption that the chain segments are rigid has been found to hinder the study of these materials at higher stretches [46,58,59]. Further, neglecting the bond distortions that contribute to internal energy, which dominates during fracture [57] poses a challenge in using the classical models for studying the fracture properties of rubber. To overcome this, Mao et al. [58] incorporated the extensibility of the molecular bonds by assuming the chain segments to be elastic. In addition to these segment stretching due to the deformation of the constituent molecular bonds, polymer chains also align in the most probable configuration upon application of a load. This statistical behavior is modeled in this study using non-Gaussian Langevin chain statistics.

In this study, each polymer chain is modeled to be made up of a number of elastic chain segments pinned to each other, as illustrated in Fig. 1. As a simplifying assumption, the properties of all the segments in each chain are assumed to be identical. For representation, an undamaged polymer chain in the initial configuration is assumed to be made up of N chain segments of length l_0 each, with a total initial contour length $L_0 = Nl_0$, as depicted in Fig. 1(a). Using the Gaussian theory, the initial end-to-end distance of the chain is determined by its root-mean-square value $R_0 = \sqrt{N}l_0$. Denoting the current end-to-end chain distance as R, the chain stretch is defined as $\lambda = R/R_0$. Due

to the extensibility of the molecular bonds, the chain segment length in the current state becomes l, and the bond stretch can be defined as $\lambda_b = l/l_0$.

Further, the Langevin parameters, which estimate the stretch in the chain, are given by

$$\Lambda = \mathcal{L}(\beta) = \frac{R}{L} = \frac{\lambda}{\lambda_b \sqrt{N}}.$$
 (1)

In the above equation, Λ and β denote the Langevin parameters, $\mathcal{L}(x) = \coth x - x^{-1}$ is the Langevin function, and L = Nl is the total current contour length of the chain. Physically, the Langevin parameter Λ is a measure of the straightness of the chain, and its unnormalized form has also been referred to as the segment realignment stretch in literature [59].

Using the Langevin statistics, the expression for the entropy of a single chain [69,70] in the current state is given by

$$s = c_0 - k_{\rm B} N \left(\beta \Lambda + \ln \frac{\beta}{\sinh \beta} \right) \,, \tag{2}$$

where, $k_{\rm B}$ represents the Boltzmann's constant and c_0 represents an arbitrary constant. Using this entropy, the expression for the total Helmholtz free energy function due to the entropy of the chain [70] is given by

$$\psi_{\text{ent}} = -T (s - s_0) = \psi_{\text{e}} - \psi_{\text{e}0}$$
 (3)

In the above equation, T represents the absolute temperature, and s_0 represents the chain entropy in the unstrained state. Ignoring the constant Tc_0 in both the terms, the expressions for the entropic free energy contributions in the current state ψ_e and the initial state ψ_{e0} are given by

$$\psi_{\rm e}(\lambda, \lambda_{\rm b}) = -Ts = k_{\rm B}TN\left(\beta\Lambda + \ln\frac{\beta}{\sinh\beta}\right) \quad \text{and} \quad \psi_{\rm e0} = \psi_{\rm e}\Big|_{\lambda=1}.$$
(4)

Additionally, the bond stretch also contributes internal energy to the total free energy of the chain. Following Talamini et al. [59] and Arunachala et al. [46], a canonical expression for the change in internal energy due to stretching in each chain segment ε_b (λ_b) is used as

$$\psi_{\text{bond}}(\lambda_{\text{b}}) = N\varepsilon_{\text{b}}(\lambda_{\text{b}}) = \frac{1}{2}NE_{\text{b}}(\lambda_{\text{b}} - 1)^{2}. \tag{5}$$

In the above equation, E_b represents the elasticity modulus of the chain segments. Using these contributions, the total free energy of an undamaged chain can be expressed as

$$\psi_{\rm ud}(\lambda, \lambda_{\rm b}) = \psi_{\rm bond}(\lambda_{\rm b}) + \psi_{\rm ent}(\lambda, \lambda_{\rm b}) = \frac{1}{2} N E_{\rm b} (\lambda_{\rm b} - 1)^2 + k_{\rm B} T N \left(\beta \Lambda + \ln \frac{\beta}{\sinh \beta}\right) - \psi_{\rm e0}. \tag{6}$$

In this study, it is assumed that the damage in the chain is not only driven by the weakening of the molecular bond attractions but also by the decrease in the entropic free energy, which is caused by an increase in the entropic freedom of the chain segments due to their softening. However, explicit changes in the structural configuration of the chain due to damage are neglected, as observed in Fig. 1(b). In line with the phase field approach, a continuous variable $d \in [0, 1]$ is assumed to represent the damaged state of the chain, with d = 0 referring to an undamaged state and d = 1 implying complete damage. Irreversibility of the damage is assumed in this study, and hence $\dot{d} \ge 0$ is enforced. Accordingly, the free energy of the damaged chain ψ_d is assumed to be obtained by the degradation of the total free energy of the chain and can be expressed as

$$\psi_{d}(\lambda, \lambda_{b}, d) = g_{chain}(d) \psi_{ud}(\lambda, \lambda_{b}). \tag{7}$$

In this equation, $g_{\text{chain}}(d)$ represents the chain degradation function and accounts for the decrease in the force response of the chain with damage. Assuming that the external power is expended only by the chain force f over the rate of stretch $\dot{\lambda}$, the expression for the polymer chain dissipation using the second law of thermodynamics can be written following Rastak and Linder [71] as

$$\mathcal{D}_{\text{chain}} = f\dot{\lambda} - \dot{\psi}_{\text{d}} = \left(f - \frac{\partial\psi_{\text{d}}}{\partial\lambda}\right)\dot{\lambda} - \frac{\partial\psi_{\text{d}}}{\partial\lambda_{\text{b}}}\dot{\lambda}_{\text{b}} - \frac{\partial\psi_{\text{d}}}{\partial d}\dot{d} \ge 0.$$
 (8)

The constitutive relations for the chain are obtained utilizing the Coleman–Noll procedure [72]. Assuming that the stretching in the chain is purely energetic, its thermodynamic conjugate force f is obtained as

$$f = \frac{\partial \psi_{\rm d}}{\partial \lambda} = g_{\rm chain}(d) k_{\rm B} T \sqrt{N} \frac{\beta}{\lambda_{\rm b}}. \tag{9}$$

As the bond stretch is assumed to be elastic, its contribution to the polymer chain dissipation is neglected. Consequently, the elastic bond stretch is obtained as the minimizer of the total damaged free energy as

$$\frac{\partial \psi_{\rm d}}{\partial \lambda_{\rm b}} = 0 \qquad \Longrightarrow \qquad \lambda_{\rm b}^2 (\lambda_{\rm b} - 1) = \frac{k_{\rm B} T}{E_{\rm b}} \beta \frac{\lambda}{\sqrt{N}} \,. \tag{10}$$

Neglecting the rate-dependent damage effects, the thermodynamic driving force for damage f_d is considered to be linearly proportional to the extent of damage in the system as

$$f_{\rm d} := -\frac{\partial \psi_{\rm d}}{\partial d} = \mathfrak{f}d. \tag{11}$$

The numerical advantages of this assumption are explained later in this section, while the rationale behind this is discussed in Section 2.3. The term $\mathfrak{f}d$ can also be viewed as the damage resistance force and can be expressed using the energetics of bond rupture. Assuming that ε_b^f is the binding energy of each monomer unit [58,59], the total amount of energy dissipated due to the breaking of N such chain segments would be $N\varepsilon_b^f$. As proposed in [59], the proportionality constant \mathfrak{f} can be evaluated by assuming the total amount of chain dissipation to be resulting from the breaking of these chain segments as

$$\int_0^\infty \mathcal{D}_{\text{chain}} dt = \int_0^\infty f_d \dot{d} dt = \frac{1}{2} f d^2 \Big|_{d=0}^{d=1} = N \varepsilon_b^f \implies \qquad \mathfrak{f} = 2N \varepsilon_b^f. \tag{12}$$

In order to obtain an expression for the damage variable d using the above form of the damage driving force, the chain degradation function is assumed to be of the form

$$g_{\text{chain}}(d) = (1 - d)^2 + \mathfrak{c}, \tag{13}$$

where c is a small positive-valued constant introduced to prevent ill-conditioning when $d \approx 1$ [25,59]. With the choice of this form of chain degradation function, elastic behavior is produced in the undamaged state as $g_{\text{chain}}(0) \approx 1$. Furthermore, a complete degradation of the stiffness is observed in the fully damaged state as $g_{\text{chain}}(1) \approx 0$, and the damage driving force f_d also vanishes as the chain attains a fully damaged state as a result of $g'_{\text{chain}}(1) = 0$. Using this form of the degradation function and Eqs. (7), (11) and (12), an explicit expression can be obtained for the damage d in the chain as

$$d = \frac{\psi_{\rm ud}}{\psi_{\rm ud} + N\varepsilon_{\rm b}^{\rm f}} \,. \tag{14}$$

The current model considers the degradation of both bond stretch and entropic energy and a linear damage driving force. The alternate formulations used in literature [33,59,61] consider one or both of the two assumptions, namely, degradation of only bond stretch internal energy and constant damage driving force. The effects of these assumptions are illustrated in Fig. 2 by juxtaposing the various aspects of the chain behavior resulting from those formulations with the chain response obtained using the current model. The constitutive relations for the chain models used for this comparison are tabulated in Table 1. The indicator function used in Table 1 is defined as

$$\mathbb{1}[x] = \begin{cases} 1 & x \text{ is True,} \\ 0 & \text{otherwise.} \end{cases}$$
(15)

As seen from Fig. 2(a), although all the models capture the softening behavior of the chains due to damage, the current model predicts a smoother response as compared to Model 2, which assumes a constant f_d . The damage predicted by the current model can be seen to be a smooth continuous function starting from zero and asymptotically reaching a value of one, as illustrated in Fig. 2(b), in line with many phase field fracture studies on elastomers [8,25,60]. This accounts for the gradual aggravation in the bond strength as compared to Model 2, wherein damage sets in abruptly when the damage driving free energy reaches a value of $N\varepsilon_b^f/2$. The current model also overcomes the discontinuous jump observed in Model 1, which considers the degradation of only bond stretch internal energy, and this is visually explained in Appendix A.

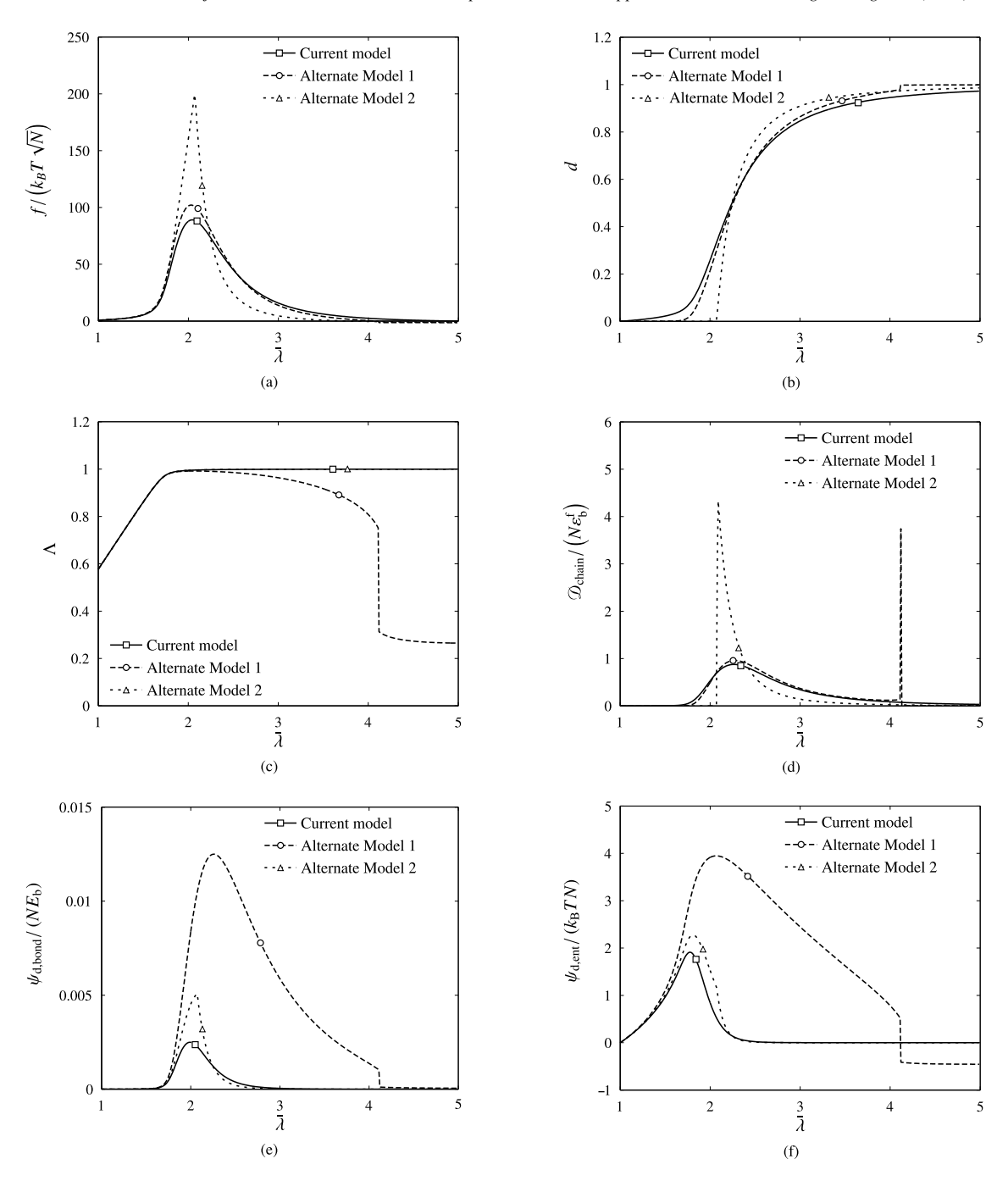


Fig. 2. Representation of the chain response to an applied stretch in terms of normalized values of (a) chain force, (b) chain damage, (c) segment realignment stretch, (d) chain dissipation, (e) bond stretch internal energy component of ψ_d , and (f) entropic free energy part of ψ_d . The current model considers degradation of both bond stretch and entropic energy, $\psi_d = g_{\text{chain}}(\psi_{\text{bond}} + \psi_{\text{ent}})$, and a linear damage driving force, $f_d = 2N\varepsilon_b^f d$. This model is compared with alternate formulations used in literature. Model 1 considers degradation of only bond stretch energy, $\psi_d = g_{\text{chain}}\psi_{\text{bond}} + \psi_{\text{ent}}$, and a linear damage driving force. Model 2 considers a constant damage driving force, $f_d = N\varepsilon_b^f$ and the degradation of both the undamaged chain free energy parts. The constitutive relations for these models are tabulated in Table 1.

The evolution of the Langevin parameter Λ in Fig. 2(c) shows that the current model predicts the chains to become straighter with the applied stretch, even though they are getting damaged. This can be considered more physically

Constitutive relations for chain models compared in 115. 2.							
Quantity	Current model	Alternate model 1	Alternate model 2				
$\psi_{ m d,bond}$	$g_{ m chain} \psi_{ m bond}$	$g_{ ext{chain}}\psi_{ ext{bond}}$	$g_{ m chain} \psi_{ m bond}$				
$\psi_{ m d,ent}$	$g_{ m chain}\psi_{ m ent}$	$\psi_{ m ent}$	g chain ψ ent				
f_{d}	$2N\varepsilon_{\mathrm{b}}^{\mathrm{f}}d$	$2Narepsilon_{ m b}^{ m f}d$	$Narepsilon_{ m b}^{ m f}$				
$\frac{f}{k_{\mathrm{B}}T\sqrt{N}}$	$g_{ m chain} rac{eta}{\lambda_{ m b}}$	$rac{eta}{\lambda_{ m b}}$	$g_{ m chain}rac{eta}{\lambda_{ m b}}$				
d	$rac{\psi_{ m ud}}{\psi_{ m ud} + N arepsilon_{ m b}^{ m f}}$	$rac{\psi_{ m ud}}{\psi_{ m ud} + N arepsilon_{ m b}^{ m f}}$	$\left(1 - \frac{N\varepsilon_{\rm b}^{\rm f}/2}{\psi_{\rm ud}}\right) \mathbb{1}\left[\psi_{\rm ud} > N\varepsilon_{\rm b}^{\rm f}/2\right]$				
$\frac{\beta}{E_{\rm h}\sqrt{N}/(k_{\rm B}T)}$	$\frac{\lambda_b^2(\lambda_b-1)}{\lambda}$	$g_{\text{chain}} \frac{\lambda_{b}^{2}(\lambda_{b}-1)}{\lambda}$	$\frac{\lambda_b^2(\lambda_b-1)}{\lambda}$				

 Table 1

 Constitutive relations for chain models compared in Fig. 2.

viable compared to the coiling due to large values of bond stretch, as predicted by Model 1. Furthermore, the current model also overcomes the discontinuous jump in the segment realignment stretch resulting from formulations in literature [65]. Although the model predicts straighter chains for larger stretch values, the increase in the entropy of the system due to the weakening of the molecular bonds is captured by the model, which can be observed from the decrease in the entropic energy part $\psi_{d,ent}$ of the total damaged free energy, as shown in Fig. 2(f). For Model 1, as the value of Λ at higher stretches is less than the initial one, the entropy is much higher at larger stretches. This results in negative values of $\psi_{d,ent}$, implying negative work of deformation done to achieve these configurations. The trend observed for entropic energy is also seen in the evolution of the bond stretch internal energy part $\psi_{d,bond}$ of the total free energy, as depicted in Fig. 2(e). The normalized $\psi_{d,bond}$ values are seen to be much lower than the corresponding normalized $\psi_{d,ent}$ values due to the large value of $E_b/(k_BT)$ considered in accordance with Talamini et al. [59].

As seen from Fig. 2(d), the current model predicts a smooth dissipation curve that follows the damage curve's slope. Model 1 also follows a similar trend, albeit with an abrupt spike due to the aforementioned discontinuous jump in the damage and Λ values. Model 2 also produces an abrupt jump at the point of damage initiation. It can be noted that the area enclosed under all three curves is equal to $N\varepsilon_b^f$.

In summary, although other studies [60,61] also assume the degradation of both the entropic and bond stretch contributions to the free energy, this work clearly highlights its advantages for modeling chain behavior. Furthermore, a non-constant damage driving force is proposed in this study, which results in a smooth, continuous chain response, and the total dissipation is assumed to be due to the breaking of the molecular bonds. The current model captures a damaged chain response overcoming the discontinuous jumps and predicts a non-decreasing segment realignment stretch for an increasing stretch, which can be considered more physically viable. The following sections deal with the description of the macroscopic damage model and the bridge linking this with the microscopic description of polymer chains within a vast random network.

2.2. Bridging micro- and macroscopic deformations using the non-affine microsphere model

For extending the microscale chain model to the macroscale, the normalized undamaged free energy and the normalized chain parameters are defined using the density of chains per unit volume n as

$$\bar{\psi}_{\rm ud} = n\psi_{\rm ud} \,, \quad \mu = nk_{\rm B}T \,, \quad E = nE_{\rm b} \,. \tag{16}$$

At the macroscale, a finite strain framework is utilized to capture rubber-like materials' behavior owing to their high stretchability. Further, due to their nearly incompressible response, a decoupled deformation gradient approach [73] is used. Accordingly, the deformation gradient F can be decomposed multiplicatively into volumetric F and isochoric F components as

$$F = F_{\text{vol}}\bar{F}$$
 where $F_{\text{vol}} = J^{1/3}I$, $\bar{F} = J^{-1/3}F$, $J = \det F > 0$. (17)

The previous section modeled the response of a single polymer chain using a one-dimensional element. However, tracking the behavior of each polymer chain in a vast network containing numerous chains oriented along different directions is impractical. Therefore, homogenizing the network using simplifying assumptions is necessary.

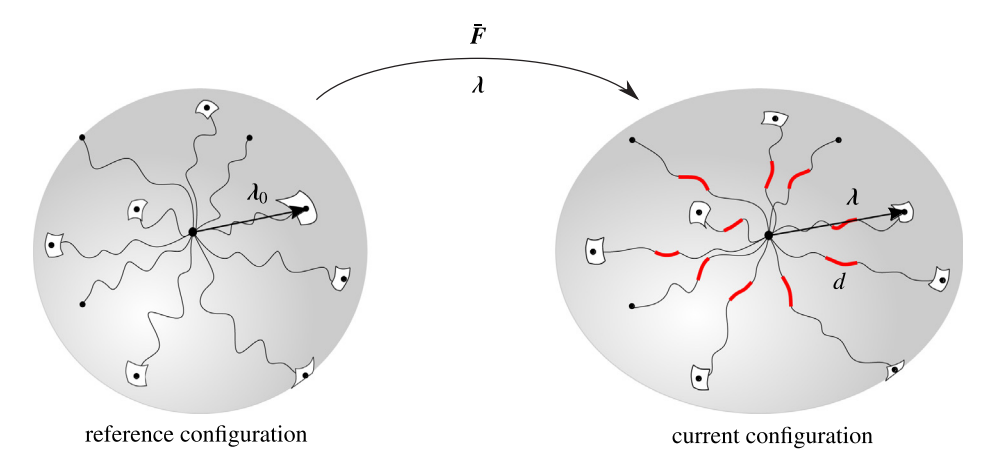


Fig. 3. Illustration of the reference and current orientation spaces of a unit volume of material containing chains oriented along different directions.

Furthermore, the macroscopic deformation should be linked to the deformation of the chains at the microscale using a suitable network model. The following explanation deals with a network homogenization method and the subsequent utilization of the non-affine microsphere model developed by Miehe et al. [50].

Following the explanation of the network homogenization method elucidated in [46,71], it is assumed that all polymer chains oriented in a specific direction λ_0 in the reference configuration share the same chain attributes, such as stretch, bond stretch, and damage. If r_0 represents the initial end-to-end vector of a chain, then its reference orientation vector is given by $\lambda_0 = r_0/|r_0|$. According to the aforementioned assumption, any two parallel chains in the reference configuration act similarly throughout any deformation because the chain properties depend solely on their reference orientations. This assumption is consistent with those used in many previous works [50,62,74,75]. Due to rubber's isotropic behavior in its undeformed configuration, the assumptions of constant chain parameters across all chains and a uniform distribution of polymer chains along all reference orientations are reasonable. This enables us to map each reference orientation onto a point on the surface \mathcal{S}_0 of a unit sphere, referred to as reference orientation space, which can be utilized in simplifying the study of random networks in a statistical manner. As a general case, assuming that the chain properties in the actual configuration vary with the reference orientation vectors, the current orientation space forms an ellipsoid, as depicted in Fig. 3. If r represents the end-to-end chain vector in the deformed configuration, the stretch vector can be obtained as $\lambda = r/|r_0|$.

A suitable network model is required to bridge these chain stretch vectors to the macroscopically observable isochoric deformation tensor \bar{F} while maintaining kinematic compatibility. The macro-stretch vector $\tilde{\lambda}$ along reference orientation λ_0 mapped by the isochoric deformation of the continuum is given by

$$\tilde{\lambda} = \bar{F}\lambda_0$$
 and $\tilde{\lambda} = |\bar{F}\lambda_0|$. (18)

In the affine deformation model [74], the chain stretch vector is assumed to be mapped from the undeformed configuration by this isochoric deformation tensor and hence, $\lambda = \tilde{\lambda}$ is considered. However, as it has been found that this strong local constraint limits the flexibility of the network and leads to an inaccurate response of the rubber material [49,76], the non-affine microsphere model developed by Miehe et al. [50] is utilized in this study.

As presented in [50], the non-affine microsphere model is a generalization of the eight-chain model by Arruda and Boyce [49], intended to extend the modeling capacity by introducing an additional material parameter. The non-affine model allows the chain stretch λ along each direction to fluctuate about their respective macro-stretch $\tilde{\lambda}$ with the help of a fluctuation field f in a multiplicative form as

$$\lambda = \tilde{\lambda} f \,. \tag{19}$$

The non-affine constraint is assumed in terms of the p-root averaging operator as

$$\langle \lambda \rangle_p = \langle \tilde{\lambda} \rangle_p \quad \text{with} \quad \langle \bullet \rangle_p = \left(\frac{1}{|\mathcal{S}_0|} \int_{\mathcal{S}_0} (\bullet)^p \, dA \right)^{1/p} .$$
 (20)

However, this constraint specifies a space of possible solutions and does not uniquely identify a single possible network response. The principle of minimum average free energy is employed to obtain a unique solution for the fluctuation field f and hence the chain stretch λ . However, from Figs. 2(e) and 2(f), it can be observed that the damaged chain energy ψ_d is not a convex function of the chain stretch λ and hence the minimization problem may not guarantee a unique solution. Therefore, the minimization of the averaged free energy of a hypothetical undamaged system is proposed in this study for obtaining a unique network response for the applied macroscopic deformation. The constrained optimization problem can be formulated as

Minimize
$$\langle \bar{\psi}_{ud} \rangle_1$$
 subject to $\langle \lambda \rangle_p = \langle \tilde{\lambda} \rangle_p$. (21)

If $\bar{\Psi}_{ud} = \langle \bar{\psi}_{ud} (\lambda, \lambda_b) \rangle_1$ represents the hypothetical average undamaged free energy of the chain, the Lagrangian form of the minimization problem (21) for calculating the chain stretch in each direction can be written as

$$L_{\rm ud}\left[\lambda,\,\nu\right] = \bar{\Psi}_{\rm ud}\left(\lambda\right) - \nu\left(\langle\lambda\rangle_p - \langle\tilde{\lambda}\rangle_p\right). \tag{22}$$

To find the stationary point of the above Lagrangian along each direction, we have

$$\frac{\partial L_{\rm ud}}{\partial \lambda} = 0 \quad \to \quad \frac{\partial \bar{\psi}_{\rm ud}}{\partial \lambda} \lambda^{1-p} = \nu \langle \lambda \rangle_p^{1-p} \,. \tag{23}$$

Since the function $\bar{\psi}_{ud}$ is convex in λ , the minimization problem is well-posed and it has been found that the above equation has a non-trivial solution only if $\lambda = \tilde{\lambda} f$ is constant along all directions [50]. From the non-affine constraint in (20), we get the closed-form solution for the equal chain stretch along all directions given by

$$\lambda = \langle \tilde{\lambda} \rangle_p \,. \tag{24}$$

On the other hand, if the average damaged free energy of the chain $\bar{\Psi}_d = \langle \bar{\psi}_d (\lambda, \lambda_b, d) \rangle_1$ is considered, the Lagrangian form of the minimization problem can be expressed as

$$L_{\rm d}\left[\lambda,\nu\right] = \bar{\Psi}_{\rm d}\left(\lambda\right) - \nu\left(\langle\lambda\rangle_p - \langle\tilde{\lambda}\rangle_p\right). \tag{25}$$

To find the stationary point of the above Lagrangian along each direction, we have

$$\frac{\partial L_{\rm d}}{\partial \lambda} = 0 \quad \to \quad \frac{\partial \bar{\psi}_{\rm d}}{\partial \lambda} \lambda^{1-p} = \nu \langle \lambda \rangle_p^{1-p} \,. \tag{26}$$

Since the function $\bar{\psi}_d$ becomes non-convex in λ as damage evolves, it leads to the ill-posedness of the minimization problem. Hence, a unique solution for the above equation is not guaranteed. However, it can be seen that the solution $\lambda = \langle \tilde{\lambda} \rangle_p$, which is constant along all directions, satisfies (26). Therefore, it can be concluded that the solution using the minimization of the undamaged free energy is also a solution if we consider the damaged system. Physically, the chain reorientations are allowed so that they achieve the lowest energy state while kinematically complying with the non-affine p-root constraint.

The Eq. (26) can have more than one solution, which can be easily seen for the special case of p=1. As $\bar{\psi}_d$ becomes non-convex with damage evolution, the equation $\partial \bar{\psi}_d/\partial \lambda = \nu$ can be satisfied at two values of λ . Thus, chain stretch values can have either of these values in different directions. Hence, a constant chain stretch along all directions is not a unique solution for the minimization problem.

Thus, an isotropic network response is predicted by this model for any macroscopic loading. In this way, the stretch in the microscale chains is bridged to the macroscopic deformation gradient and this mapping helps in extending the microscale chain model to a continuum model.

2.3. Macroscale damage model

The previous sub-sections describe the total free energy for a damaged chain and the mapping between the microscale chain stretch and the macroscale deformation gradient. Using these, the single-chain model can be extended to a macroscale continuum model. As a convention, the derivatives in the reference configuration are denoted as

$$\operatorname{Div}\left(\bullet\right) = \frac{\partial}{\partial X} \cdot \left(\bullet\right) \; ; \quad \nabla_{X}\left(\bullet\right) = \frac{\partial}{\partial X} \left(\bullet\right) \; ; \quad \Delta_{X}\left(\bullet\right) = \frac{\partial}{\partial X} \cdot \frac{\partial}{\partial X} \left(\bullet\right) \; . \tag{27}$$

Similarly, the derivatives in the current configuration are represented as

$$\operatorname{div}(\bullet) = \frac{\partial}{\partial x} \cdot (\bullet) \; ; \quad \nabla_x(\bullet) = \frac{\partial}{\partial x} (\bullet) \; ; \quad \Delta_x(\bullet) = \frac{\partial}{\partial x} \cdot \frac{\partial}{\partial x} (\bullet) \; . \tag{28}$$

In the above equations, X and x represent the positions of the material points in the reference and current configurations, respectively. As a result of the isotropic network response predicted by the microsphere model, it is reasonable to assume that the chain damage and bond stretch values are constant in chains along all directions. Hence, a single damage field d is assumed to represent the damage at both scales, similar to other works in literature [33,59,60]. Similarly, the macroscopic variable representing the bond stretch in chains along all directions can be considered as λ_b . The free energy of the chains along all the directions is constant and hence the macroscale free energy contribution due to the chains is given by $\langle \bar{\psi}_d \rangle_1 = \bar{\psi}_d$.

As mentioned in Section 2.2, the volumetric and isochoric responses of the material at the continuum level are separated, and the chain deformations are assumed to affect the isochoric part only. As a result of the slight compressibility of the material, the free energy contribution due to the volumetric changes is accounted for, and the bulk free energy expression is assumed as

$$U_{\text{bulk}}(J) = \frac{1}{8}K\left(J - \frac{1}{J}\right)^2,\tag{29}$$

in line with many works in literature [59,77,78]. The parameter K represents the bulk modulus of the material. The degradation of this bulk free energy is assumed to be of the form

$$g_{\text{bulk}}(d) = (1-d)^3 + \gamma_{\text{bulk}} c.$$
 (30)

A cubic degradation of the bulk is assumed for degrading the bulk modulus K faster than the shear modulus μ [60], and this eases the incompressibility constraint on the highly stretched damaged regions for overcoming numerical issues. The small positive-valued constant \mathfrak{c} is also scaled by a constant $\gamma_{\text{bulk}} = (\mu/K)$ for numerical stability, following Kumar et al. [36]. Further, the nonlocal nature of the damage is captured following Talamini et al. [59] as

$$\Psi_{\text{nonlocal}}(\nabla_X d) = \bar{\varepsilon}_b^f \ell^2 |\nabla_X d|^2, \tag{31}$$

wherein ℓ represents an intrinsic length scale for the damage process. The chain scission energy when all bonds are broken is given by the expression

$$\bar{\varepsilon}_{\rm h}^{\rm f} = nN\varepsilon_{\rm h}^{\rm f}$$
 (32)

The above equation assumes negligible interaction between the polymer chains; hence, the effects of van der Waal's forces and even bond angle rotations are neglected. The above expression also implies a simultaneous failure of all the chain segments in a unit volume, which is reasonable as we assume the chains to be made up of identical chain segments. Additionally, the thermal fluctuations in the chain, which may lead to failure at a single bond, are also neglected, considering the fact that the monomer binding energy is much larger than the average thermal energy at usual operating temperatures [59]. As the internal energy due to molecular bond distortions dominates during the rupture of polymers [57], the critical free energy at rupture $\bar{\Psi}_{cr}$ can be approximated as the bond rupture energy $\bar{\varepsilon}_b^f$. Using this fact, the order of magnitude of the length scale ℓ for a material can be approximated based on the work by Thomas [79], using the critical energy release rate G_c and the bond rupture energy $\bar{\varepsilon}_b^f$ as

$$\ell \sim G_c/\bar{\Psi}_{\rm cr} \sim G_c/\bar{\varepsilon}_{\rm b}^{\rm f}$$
 (33)

Accounting for the bulk free energy, contribution by the microscale chains, and the nonlocal damage effects, the total macroscale free energy of the system is proposed as

$$\Psi\left(F, \lambda_{b}, d, \nabla_{X} d\right) = g_{\text{bulk}}\left(d\right) U_{\text{bulk}}\left(J\right) + g_{\text{chain}}\left(d\right) \bar{\psi}_{\text{ud}}(\lambda, \lambda_{b}) + \bar{\varepsilon}_{b}^{f} \ell^{2} \left|\nabla_{X} d\right|^{2}. \tag{34}$$

The balance laws of mass, linear momentum, angular momentum, micro-forces, and the laws of thermodynamics are utilized for obtaining the constitutive and governing equations. The complete derivation is expounded in Appendix B.

In terms of the Kirchhoff stress tensor τ , the governing equation obtained from the balance of linear momentum is given by

$$\operatorname{div}\left(\frac{1}{J}\tau\right) = 0. \tag{35}$$

Assuming the damage variable to be associated with the internal micro-force π_d and the micro-stress vector ξ_d , micro-force balance leads to

$$\operatorname{Div} \boldsymbol{\xi}_{d} + \pi_{d} = 0. \tag{36}$$

Assuming the bond stretch variable to be associated with the internal micro-force π_b , the micro-force balance leads to

$$\pi_{\mathsf{b}} = 0. \tag{37}$$

The simplified form of the dissipation inequality obtained using the laws of thermodynamics can be expressed as

$$\tau: \mathbf{D} + \boldsymbol{\xi}_{d} \cdot \nabla_{\mathbf{X}} \dot{d} - \pi_{d} \dot{d} - \pi_{b} \dot{\lambda}_{b} - \dot{\Psi} \ge 0, \tag{38}$$

wherein, D represents the rate of deformation tensor. The above dissipation inequality can be evaluated for the form of the free energy function in (34) as

$$\left(\boldsymbol{\tau} - 2\frac{\partial \Psi}{\partial \boldsymbol{g}}\right) : \boldsymbol{D} + \left(\boldsymbol{\xi}_{d} - \frac{\partial \Psi}{\partial \nabla_{\boldsymbol{X}} d}\right) \cdot \nabla_{\boldsymbol{X}} \dot{d} - \left(\boldsymbol{\pi}_{d} + \frac{\partial \Psi}{\partial d}\right) \dot{d} - \left(\boldsymbol{\pi}_{b} + \frac{\partial \Psi}{\partial \lambda_{b}}\right) \dot{\lambda}_{b} \ge 0.$$
(39)

In the above equation, g is the Eulerian metric tensor. The dissipation can be assumed to be mainly due to the rupture of monomer molecular bonds. Similar to Talamini et al. [59], we consider the internal damage micro-force π_d to be made up of energetic and dissipative parts. As the other quantities do not contribute to dissipation, it can be assumed that they are purely energetic. Applying the Coleman–Noll procedure [72], we obtain

$$\boldsymbol{\tau} = 2\frac{\partial \Psi}{\partial \boldsymbol{g}}; \quad \boldsymbol{\xi}_{d} = \frac{\partial \Psi}{\partial \nabla_{\boldsymbol{X}} d}; \quad \boldsymbol{\pi}_{d,en} = -\frac{\partial \Psi}{\partial d}; \quad \boldsymbol{\pi}_{b} = -\frac{\partial \Psi}{\partial \lambda_{b}}. \tag{40}$$

The dissipative part of the internal damage micro-force can be assumed as

$$\pi_{d\,diss} = -\left(2\bar{\varepsilon}_b^f d + \zeta \dot{d}\right) \,. \tag{41}$$

In the above equation, ζ is a material parameter accounting for the rate-dependent damage effects. The form of the rate-independent term is similar to that discussed in Section 2.1. Using Eqs. (34), (36), (40) and (41), the governing equation for the damage field d is obtained as

$$2\bar{\varepsilon}_{b}^{f}(\ell^{2}\Delta_{X}d - d) = g'_{bulk}(d) U_{bulk}(J) + g'_{chain}(d) \bar{\psi}_{ud}(\lambda, \lambda_{b}) + \zeta \dot{d}.$$

$$(42)$$

For accounting for the irreversibility in damage, free energy history variables are introduced for the bulk and undamaged chain free energies following Miehe et al. [80] as

$$\mathcal{H}_{\text{bulk}}\left(J(t)\right) = \max_{s \in [0,t]} U_{\text{bulk}}\left(J(s)\right) \quad \text{and} \quad \mathcal{H}_{\text{chain}}\left(\lambda(t), \lambda_{\text{b}}(t)\right) = \max_{s \in [0,t]} \bar{\psi}_{\text{ud}}\left(\lambda(s), \lambda_{\text{b}}(s)\right) \,. \tag{43}$$

The necessity and effectiveness of these history variables in maintaining the fracture irreversibility criterion are proved in Appendix C using a local damage model in a one-dimensional setting, following Miehe et al. [80]. Using these history variables in (42), the governing equation for the damage field is obtained as

$$2\bar{\varepsilon}_{b}^{f}(\ell^{2}\Delta_{X}d - d) = g'_{bulk}(d)\,\mathcal{H}_{bulk} + g'_{chain}(d)\,\mathcal{H}_{chain} + \zeta\dot{d}\,. \tag{44}$$

Remark 1. It can be observed that the form of (44) resembles the equation obtained by Miehe and Schänzel [25], who started with a crack surface functional by assuming regularization of a sharp crack using an exponential function. This results from the linear form of damage driving force proposed in this formulation, thus explaining the rationale behind this assumption. Although the study by Miehe and Schänzel [25] establishes the relationship between the fracture toughness and the average bond dissociation energy, it must be noted that the current micromechanically motivated model fundamentally differs from that developed by Miehe and Schänzel [25]. In the proposed model, macroscale damage is driven by a significant contribution from the internal energy due to the molecular stretching at the microscale. At the same time, the work by Miehe and Schänzel [25] assumes the damage to be driven by the phenomenological hyperelastic free energy.

The constitutive relation for the bond stretch variable can be obtained using Eqs. (37) and (40) as

$$\frac{\partial \Psi}{\partial \lambda_{b}} = 0 \quad \rightarrow \quad \frac{\partial \bar{\Psi}_{ud}}{\partial \lambda_{b}} = 0 \,, \tag{45}$$

recovering the form (10) obtained in microscale formulation, but normalized with chain density per unit volume n. With the governing equations for the displacement field in (35), the damage field in (44) and the constitutive relation for the bond stretch internal variable in (45), the continuum model can be numerically implemented using the finite element method.

3. Numerical implementation

The proposed model is numerically implemented using the finite element method. As the gradient effects of the damage are considered in the model, it cannot be solved locally at the element level. Therefore, in addition to the displacements, the damage variable is also considered as an unknown degree of freedom. Due to its reduced simulation time, the monolithic scheme is chosen over the staggered scheme for solving the global system. The subsequent explanation delves into the details of the implementation at the Gauss point and element levels at the current time step t_{n+1} .

3.1. Gauss point level

At each Gauss point, the constitutive relations are utilized for computing the relevant quantities like stress and consistent tangent modulus, which are later required for computations at the element level. At each nonlinear iteration loop of the finite element simulation, the initial values of the degrees of freedom u, d are available as the inputs. Using this, the deformation gradient is calculated and further decomposed into volumetric and isochoric parts using (17).

First, the chain stretch λ is computed based on the isochoric deformation gradient \bar{F} using the microsphere model. As the model requires computing the p-root average of the affine stretch over the orientation space, the numerical integration scheme for symmetric functions over a unit sphere proposed by Bažant and Oh [81] is utilized. Accordingly, $n_{\text{int}}=21$ discrete quadrature directions are considered for the initial chain orientations in the undeformed configuration, and along each integration direction λ_0^{α} , the macro-stretch $\tilde{\lambda}^{\alpha}$ is calculated using (18) as

$$\tilde{\lambda}^{\alpha} = |\bar{F}\lambda_0^{\alpha}|. \tag{46}$$

The chain stretch λ , which is equal in all directions, is calculated using (24) as

$$\lambda = \langle \tilde{\lambda} \rangle_p = \left(\sum_{\alpha=1}^{n_{\text{int}}} W^{\alpha} \left(\tilde{\lambda}^{\alpha} \right)^p \right)^{1/p} , \tag{47}$$

where W^{α} represents the weight coefficient associated with the α th orientation direction. With the help of this chain stretch λ , the bond stretch λ_b in the chains can be calculated. As the equation for solving λ_b is nonlinear, Newton–Raphson algorithm is employed and iterations are performed to minimize the residual expression considered as

$$R_{\rm b} = \frac{\lambda}{\left(\lambda_{\rm b}\sqrt{N}\right)} - \Lambda \,. \tag{48}$$

In the above equation, the Langevin parameters are calculated using the result from (45) as

$$\Lambda = \coth \beta - \beta^{-1} \qquad \beta = \frac{E}{\mu} \lambda_b^2 (\lambda_b - 1) \frac{\sqrt{N}}{\lambda}. \tag{49}$$

The tangent for the iteration loop is obtained as

$$K_{\rm b} = -\frac{\mathrm{d}R_{\rm b}}{\mathrm{d}\lambda_{\rm b}} = \frac{\lambda}{\lambda_{\rm b}^2 \sqrt{N}} + \mathcal{L}'(\beta) \frac{E}{\mu} \left(3\lambda_{\rm b}^2 - 2\lambda_{\rm b} \right) \frac{\sqrt{N}}{\lambda} \,. \tag{50}$$

The above expression's derivation considers that the chain stretch λ remains constant during the iteration loop. For a faster convergence, the bond stretch λ_b value at the previous time step t_n is used as the initial guess. With the help of the chain stretch λ and bond stretch λ_b values, the total undamaged free energy of the chain is calculated similar to (6) as

$$\bar{\psi}_{\rm ud}(\lambda, \lambda_{\rm b}) = \frac{1}{2} NE (\lambda_{\rm b} - 1)^2 + \mu N \left(\beta \Lambda + \ln \frac{\beta}{\sinh \beta} \right) - \bar{\psi}_{\rm e0} \quad \text{with} \quad \bar{\psi}_{\rm e0} = \mu N \left(\beta \Lambda + \ln \frac{\beta}{\sinh \beta} \right) \Big|_{\lambda = 1}. \tag{51}$$

Using the Jacobian J and the input damage values d, the bulk free energy function U_{bulk} and the degradation functions g_{bulk} , g_{chain} are computed using Eqs. (29), (30) and (13). Using the values of the free energy history variables at the previous time step $\mathcal{H}_{\text{bulk},n}$, $\mathcal{H}_{\text{chain},n}$, the current step values are updated according to (43) as

$$\mathcal{H}_{\text{bulk}} = \max \left\{ U_{\text{bulk}}, \mathcal{H}_{\text{bulk},n} \right\} \quad \text{and} \quad \mathcal{H}_{\text{chain}} = \max \left\{ \bar{\psi}_{\text{ud}}, \mathcal{H}_{\text{chain},n} \right\}.$$
 (52)

The undamaged isochoric Kirchhoff stress tensor can be obtained from the undamaged chain free energy (51) as

$$\bar{\boldsymbol{\tau}}_{\mathrm{ud}} = 2 \frac{\partial \bar{\psi}_{\mathrm{ud}}}{\partial \boldsymbol{g}} = E N \lambda_{\mathrm{b}} \left(\lambda_{\mathrm{b}} - 1 \right) \lambda^{-p} \tilde{\boldsymbol{h}} \,. \tag{53}$$

The corresponding undamaged isochoric consistent tangent modulus is obtained as

$$\bar{\mathbb{C}}_{\mathrm{ud}} = 2\frac{\partial \bar{\boldsymbol{\tau}}_{\mathrm{ud}}}{\partial \boldsymbol{g}} = EN\lambda^{-p} \left[\left((2\lambda_{\mathrm{b}} - 1) \, k_{\lambda_{\mathrm{b}}\lambda} - p \frac{\lambda_{\mathrm{b}} \, (\lambda_{\mathrm{b}} - 1)}{\lambda} \right) \lambda^{1-p} \tilde{\boldsymbol{h}} \otimes \tilde{\boldsymbol{h}} + (p-2) \, \lambda_{\mathrm{b}} \, (\lambda_{\mathrm{b}} - 1) \, \tilde{\mathbb{H}} \right]. \tag{54}$$

In the above equation, the tensors \tilde{h} , $\tilde{\mathbb{H}}$ obtained using the macro-stretch are given by

$$\tilde{\boldsymbol{h}} = \langle \tilde{\lambda}^{p-2} \tilde{\boldsymbol{\lambda}} \otimes \tilde{\boldsymbol{\lambda}} \rangle_{1} \quad \text{and} \quad \tilde{\mathbb{H}} = \langle \tilde{\lambda}^{p-4} \tilde{\boldsymbol{\lambda}} \otimes \tilde{\boldsymbol{\lambda}} \otimes \tilde{\boldsymbol{\lambda}} \otimes \tilde{\boldsymbol{\lambda}} \rangle_{1}. \tag{55}$$

Assuming that the Newton iteration loop for solving the bond stretch gets converged, it is reasonable to assume $R_b = dR_b = 0$ after the convergence of the loop. The total change in this residual can be written as

$$dR_{b} = \frac{\partial R_{b}}{\partial \lambda} d\lambda + \frac{\partial R_{b}}{\partial \lambda_{b}} d\lambda_{b} = k_{R_{b}\lambda} d\lambda + k_{R_{b}\lambda_{b}} d\lambda_{b} = 0.$$
(56)

Using the above expansion, the stiffness term $k_{\lambda h \lambda}$ used in (54) can be calculated as

$$k_{\lambda_{b}\lambda} = \frac{\partial \lambda_{b}}{\partial \lambda} \bigg|_{R_{b}=0} = -\frac{k_{R_{b}\lambda}}{k_{R_{b}\lambda_{b}}} = \frac{1}{K_{b}} \left(\frac{1}{\lambda_{b}\sqrt{N}} + \mathcal{L}'(\beta) \frac{E}{\mu} \lambda_{b}^{2} (\lambda_{b} - 1) \frac{\sqrt{N}}{\lambda^{2}} \right).$$
 (57)

Considering the degradation and the bulk free energy, the total Kirchhoff stress can be computed as

$$\boldsymbol{\tau} = 2\frac{\partial \Psi}{\partial \boldsymbol{\sigma}} = g_{\text{bulk}}(d)\,\boldsymbol{\mathfrak{p}}\boldsymbol{I} + g_{\text{chain}}(d)\,\boldsymbol{\bar{\tau}}_{\text{ud}}: \mathbb{P}\,,\tag{58}$$

and the corresponding total consistent tangent modulus can be computed following Miehe et al. [50] as

$$\mathbb{C} = 2\frac{\partial \boldsymbol{\tau}}{\partial \boldsymbol{g}} = g_{\text{bulk}}(d) \left[(\mathfrak{p} + \mathfrak{K}) \boldsymbol{I} \otimes \boldsymbol{I} - 2\mathfrak{p}\mathbb{I} \right] + g_{\text{chain}}(d)$$

$$\times \left[\mathbb{P}^{T} : \left(\bar{\mathbb{C}}_{\text{ud}} + \frac{2}{3} \left(\bar{\boldsymbol{\tau}}_{\text{ud}} : \boldsymbol{I} \right) \mathbb{I} \right) : \mathbb{P} - \frac{2}{3} \left(\mathbb{P}^{T} : \bar{\boldsymbol{\tau}}_{\text{ud}} \otimes \boldsymbol{I} + \boldsymbol{I} \otimes \bar{\boldsymbol{\tau}}_{\text{ud}} : \mathbb{P} \right) \right].$$
(59)

In the above equations, $I = \delta_{ij}$ is the second order identity tensor, $\mathbb{I}_{ijkl} = \frac{1}{2} \left(\delta_{ik} \delta_{jl} + \delta_{il} \delta_{jk} \right)$ represents the symmetric fourth order identity tensor and $\mathbb{P} = \mathbb{I} - \frac{1}{3} I \otimes I$ is the fourth order projection tensor. The terms \mathfrak{p} and \mathfrak{K} are given by

$$\mathfrak{p} = JU'_{\text{bulk}}(J) \quad \text{and} \quad \mathfrak{K} = J^2 U''_{\text{bulk}}(J) . \tag{60}$$

3.2. Element level

At the element level, the residuals and the tangent stiffness matrices are calculated for the nonlinear iterations. First, the weak forms of the governing equations for the displacement u and damage d degrees of freedom are

derived. Using δu to represent the variations in the displacement degrees of freedom, the weak form of their governing equation is obtained using (35) as

$$\int_{V} \operatorname{div} \left(\frac{1}{J} \boldsymbol{\tau} \right) \cdot \delta \boldsymbol{u} \, dV = 0 \quad \rightarrow \quad \int_{A_{0t}} \boldsymbol{\tau} \boldsymbol{n} \cdot \delta \boldsymbol{u} \, dA_{0} - \int_{V_{0}} \boldsymbol{\tau} : \nabla_{x} \delta \boldsymbol{u} \, dV_{0} = 0 \,, \tag{61}$$

wherein, V_0 and V represent the body in the reference and current configurations respectively, and A_{0t} indicates the boundaries in the reference configuration on which Neumann boundary conditions are prescribed, as explained in Appendix B. Using δd to represent the variations in the damage degree of freedom, the weak form of its governing equation is obtained using (44) as

$$\int_{V_0} \left[2\bar{\varepsilon}_b^f(\ell^2 \Delta_X d - d) - g'_{\text{bulk}}(d) \mathcal{H}_{\text{bulk}} - g'_{\text{chain}}(d) \mathcal{H}_{\text{chain}} - \zeta \dot{d} \right] \delta d \, dV_0 = 0.$$
 (62)

To simplify the above equation, the boundary condition

$$\nabla_X d \cdot N = 0 \quad \text{on } A_0 \tag{63}$$

is imposed on all boundaries A_0 in reference configuration, for driving the damage only by mechanical loading and not by any other external boundary conditions [82]. The time derivative is numerically approximated as $\dot{d} \approx (d - d_n)/\Delta t$ using the damage value d_n at the previous time step and the time increment Δt . Using these, the simplified form of (62) is given by

$$-\int_{V_0} \left[2\bar{\varepsilon}_{b}^{f} \ell^2 \nabla_X d \cdot \nabla_X \delta d + \left(2\bar{\varepsilon}_{b}^{f} d + g'_{\text{bulk}}(d) \mathcal{H}_{\text{bulk}} + g'_{\text{chain}}(d) \mathcal{H}_{\text{chain}} + \zeta \frac{d - d_n}{\Delta t} \right) \delta d \right] dV_0 = 0.$$
 (64)

The spatial discretization of the weak forms is performed using the Galerkin method. In each element of the finite element simulation, both the displacement u and the damage d degrees of freedom are approximated using the same set of shape functions as

$$u_i = \sum_{A=1}^{n_{\text{nodes}}} N^A \bar{u}_i^A \quad \text{and} \quad d = \sum_{A=1}^{n_{\text{nodes}}} N^A \bar{d}^A \,, \tag{65}$$

wherein N^A represents the spatially varying shape function at node A in the element domain, while \bar{u}_i^A and \bar{d}^A denote the discrete ith component of the nodal displacement and discrete nodal damage values at node A respectively. Note that Einstein index notation is employed for representing the components in the current and reference configurations. In a Bubnov Galerkin context, the same shape functions are used to approximate their variations at the elemental level as well and can be written as

$$\delta u_i = \sum_{A=1}^{n_{\text{nodes}}} N^A \delta \bar{u}_i^A \quad \text{and} \quad \delta d = \sum_{A=1}^{n_{\text{nodes}}} N^A \delta \bar{d}^A \,. \tag{66}$$

Using these discretizations, the residual expressions at the element level for the unknown degrees of freedom can be calculated. Assuming that the traction boundary term is calculated separately only on the boundary elements, the general element residual equation for the displacement degrees of freedom is obtained using (61) as

$$(R_{\mathbf{u}}^{\mathbf{e}})_{i}^{A} = -\int_{V_{0}^{\mathbf{e}}} \tau_{ij} N_{,j}^{A} \, \mathrm{d}V_{0} \,. \tag{67}$$

In the above equation, $V_0^{\rm e}$ represents the discretized element domain in the reference configuration. The element residual equation for the damage degree of freedom is obtained using (64) as

$$\left(R_{\rm d}^{\rm e}\right)^{A} = -\int_{V_{\rm c}^{\rm e}} \left[2\bar{\varepsilon}_{\rm b}^{\rm f}\ell^{2}d_{,K}N_{,K}^{A} + \left(2\bar{\varepsilon}_{\rm b}^{\rm f}d + g_{\rm bulk}^{\prime}\left(d\right)\mathcal{H}_{\rm bulk} + g_{\rm chain}^{\prime}\left(d\right)\mathcal{H}_{\rm chain} + \zeta\frac{d - d_{n}}{\Delta t}\right)N^{A}\right] dV_{0}. \tag{68}$$

As the residuals are coupled in terms of the unknown fields, the coupled element tangent stiffness matrix composed of K_{uu}^e , K_{ud}^e , K_{du}^e and K_{dd}^e components needs to be computed. First, the K_{uu}^e term is composed of material and geometric parts, and is derived using (67) as

$$(K_{\text{uu,m}}^{\text{e}})_{ij}^{AB} = \int_{V_0^{\text{e}}} N_{,k}^{A} \mathbb{C}_{ikjl} N_{,l}^{B} \, dV_0 \quad \text{and} \quad (K_{\text{uu,g}}^{\text{e}})_{ij}^{AB} = \int_{V_0^{\text{e}}} N_{,k}^{A} \tau_{kl} \delta_{ij} N_{,l}^{B} \, dV_0.$$
 (69)

The component $K_{\rm nd}^{\rm e}$ is also derived using (67) as

$$(K_{\rm ud}^{\rm e})_{i}^{AB} = \int_{V_{0}^{\rm e}} N_{,k}^{A} (g_{\rm bulk}^{'}(d) \, \mathfrak{p} \delta_{ik} + g_{\rm chain}^{'}(d) \, (\bar{\tau}_{\rm ud})_{mn} \, \mathbb{P}_{mnik}) \, N^{B} \, \mathrm{d}V_{0} \,.$$
 (70)

The coupled component $K_{\rm du}^{\rm e}$ is calculated using (68) as

$$\left(K_{\text{du}}^{e}\right)_{j}^{AB} = \int_{V_{0}^{e}} N^{A} \left(g_{\text{bulk}}^{\prime}\left(d\right) \mathbb{1}\left[\mathcal{H}_{\text{bulk}} > \mathcal{H}_{\text{bulk,n}}\right] \mathfrak{p} \delta_{jk} + g_{\text{chain}}^{\prime}\left(d\right) \mathbb{1}\left[\mathcal{H}_{\text{chain}} > \mathcal{H}_{\text{chain,n}}\right] (\bar{\tau}_{\text{ud}})_{mn} \mathbb{P}_{mnjk}\right) N_{,k}^{B} \, dV_{0} \,.$$

$$(71)$$

In the above equation, the indicator function is defined as in (15). The final component $K_{\rm dd}^{\rm e}$ is also obtained using (68) as

$$\left(K_{\rm dd}^{\rm e}\right)^{AB} = \int_{V_0^{\rm e}} \left[2\bar{\varepsilon}_{\rm b}^{\rm f}\ell^2 N_{,K}^A N_{,K}^B + \left(2\bar{\varepsilon}_{\rm b}^{\rm f} + g_{\rm bulk}^{\prime\prime}\left(d\right)\mathcal{H}_{\rm bulk} + g_{\rm chain}^{\prime\prime}\left(d\right)\mathcal{H}_{\rm chain} + \zeta \frac{1}{\Delta t}\right) N^A N^B\right] \mathrm{d}V_0. \tag{72}$$

The above residual and stiffness terms can be assembled over all elements in order to obtain the global residual vector and stiffness matrix. At each time step, the values of damage d, damage driving free energy history variables $\mathcal{H}_{\text{bulk}}$, $\mathcal{H}_{\text{chain}}$ and bond stretch λ_b at each Gauss point are stored as history variables, and are provided as inputs to the next time step. The integrals at the element level are computed using the Gaussian quadrature rule and the required quantities at the Gauss point level are computed as shown in Section 3.1. This model is implemented using the finite element framework MOOSE [83] and the high performance tensor library Fastor [84] is used for performing tensor manipulations. Finally, the model is validated by performing three-dimensional simulations and comparing the predictions with experimental data present in literature.

4. Numerical results

For validating the proposed model, numerical simulations are performed and the predictions are compared with the experimental data. First, the experimental data for a double-edge notched specimen under tensile loading by Hocine et al. [15] is studied to verify the capability of the model to capture simple crack paths and estimate the load–displacement behavior. For corroborating the ability of the model to accurately predict fracture nucleation and complex crack paths in inhomogeneous systems, a rectangular film embedded with rigid inclusions and subjected to uniaxial tensile loading is considered. The experimental load–displacement behavior and the crack propagation paths presented in [85] are utilized for validating the model predictions. Finally, the effect of the length scale parameter on the model's predictive ability of fracture behavior is discussed.

In the following examples, three-dimensional simulations are performed by discretizing the specimen model using brick elements. Additionally, the adaptive time-stepping feature of *MOOSE* is leveraged for optimizing the simulation runtime.

4.1. Double-edge notch tensile specimen

The experimental data by Hocine et al. [15] for the fracture behavior of double-edge notched thin sheets of styrene-butadiene rubber (SBR) subjected to uniaxial tension, as shown in Fig. 4, is used for this study. The dimensions of the specimen, illustrated in Fig. 4(a), are 80 mm \times 200 mm \times 3 mm, with cracks of different lengths $a_c = 12$, 16, 20, 24, and 28 mm considered for the study. Similar to Talamini et al. [59] and Arunachala et al. [46], the notch tip is considered to have a very small root radius as a modeling assumption. This initial root radius is chosen to be R = 1 mm, which is a small value compared to the dimensions of the specimen, for computational tractability. Leveraging the symmetry, only one-eighth of the specimen is modeled for the simulations. The boundary conditions include fixed bottom and top edges, while the top edge is provided a vertical strain at a rate of 1×10^{-3} s⁻¹.

The material parameters tabulated in Table 2 are calibrated for $a_c = 16$ mm case and the same set is used for the other cases too. The microscale parameters μ , N, and E, and the non-affinity parameter p are calibrated based on the pre-peak behavior. The value of the shear modulus μ is in line with those used in previous studies [25,59]. Although Talamini et al. [59] required a large value of parameter N for modeling the Neo-Hookean behavior, we

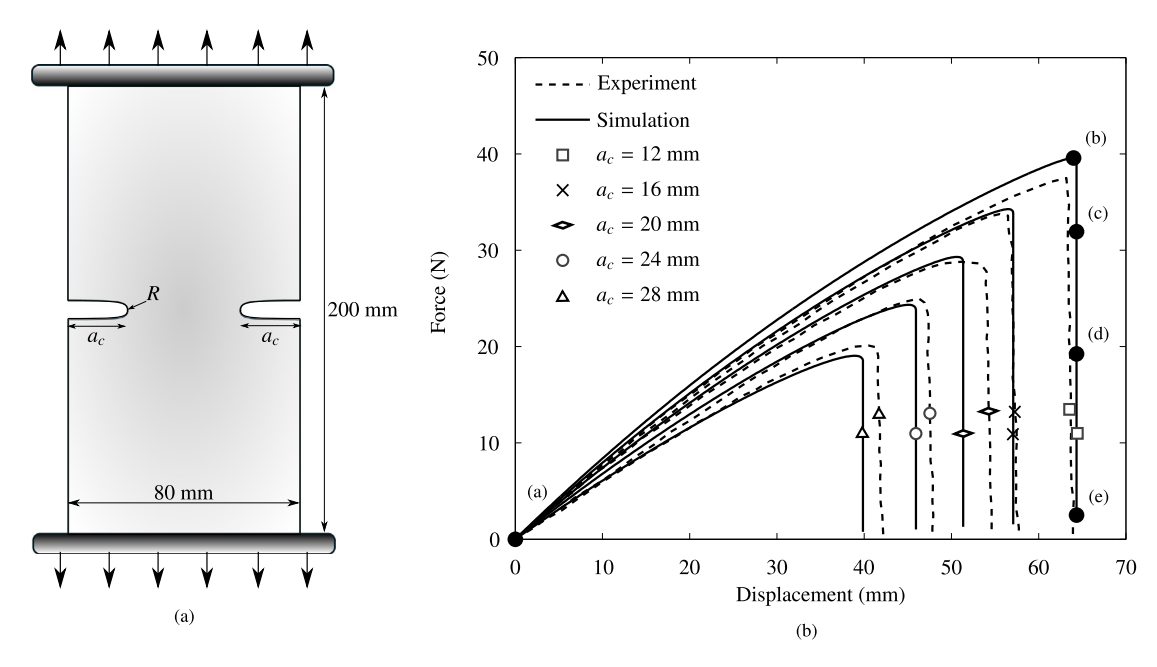


Fig. 4. Double-edge notched specimen in tension. (a) Geometry of the specimen; (b) Force-displacement response compared with the experimental results by Hocine et al. [15]. The text labels on the load-displacement curve for $a_c = 12$ mm specimen indicate the different stages of the simulation at which the damage contours in Figs. 5 and 6 are depicted.

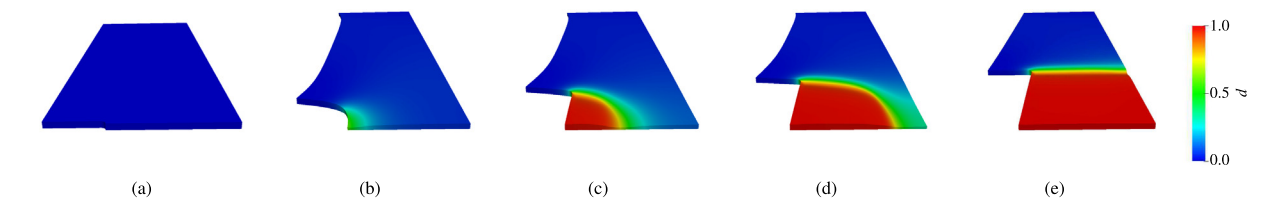


Fig. 5. Evolution of damage in 3D for the case of $a_c = 12$ mm at different stages of the simulation as depicted in Fig. 4(b). Symmetry is leveraged and only 1/8th of the specimen is utilized for simulations.

 Table 2

 Parameters used for the double edge notch tensile specimen.

μ	N	E	p	K	$ar{arepsilon}_{ m b}^{ m f}$	ℓ	ζ
0.245 MPa	20	12 MPa	2.0	10 MPa	0.9 MPa	2 mm	10^{-3} s^{-1}

use a more physically viable value of N, similar to Arunachala et al. [46]. The choice of the length scale parameter ℓ is made based on the dimensions of the specimen, and mesh elements are refined to a size of $\ell/10$ along the expected crack path. The critical energy release rate values G_c at crack initiation are estimated using the J-integral in [15] and the average value is reported as $J_c = 1.26 \text{ kJ/m}^2$. The value of the bond rupture energy $\bar{\epsilon}_b^f$ is chosen such that the relation (33) is approximately satisfied. As a sudden force drop is observed in the post-peak segment of the load–displacement curves, a small value of ζ is chosen. The value of the small positive constant \mathfrak{c} used in the degradation functions is taken as 10^{-3} for these simulations.

The resulting force–displacement curves obtained from the simulations compare well with the experimental data, as shown in Fig. 4(b). The evolution of the damage on the 3D deformed shape is visualized in Fig. 5. Due to a large value of bulk modulus K, the high-strain regions near the notch tip exhibit large out-of-plane contractions to maintain the quasi-incompressibility condition. However, as damage evolves, the incompressibility constraint is weakened as a result of the degradation in the bulk modulus due to $g_{\text{bulk}}(d)$. Therefore, the highly damaged

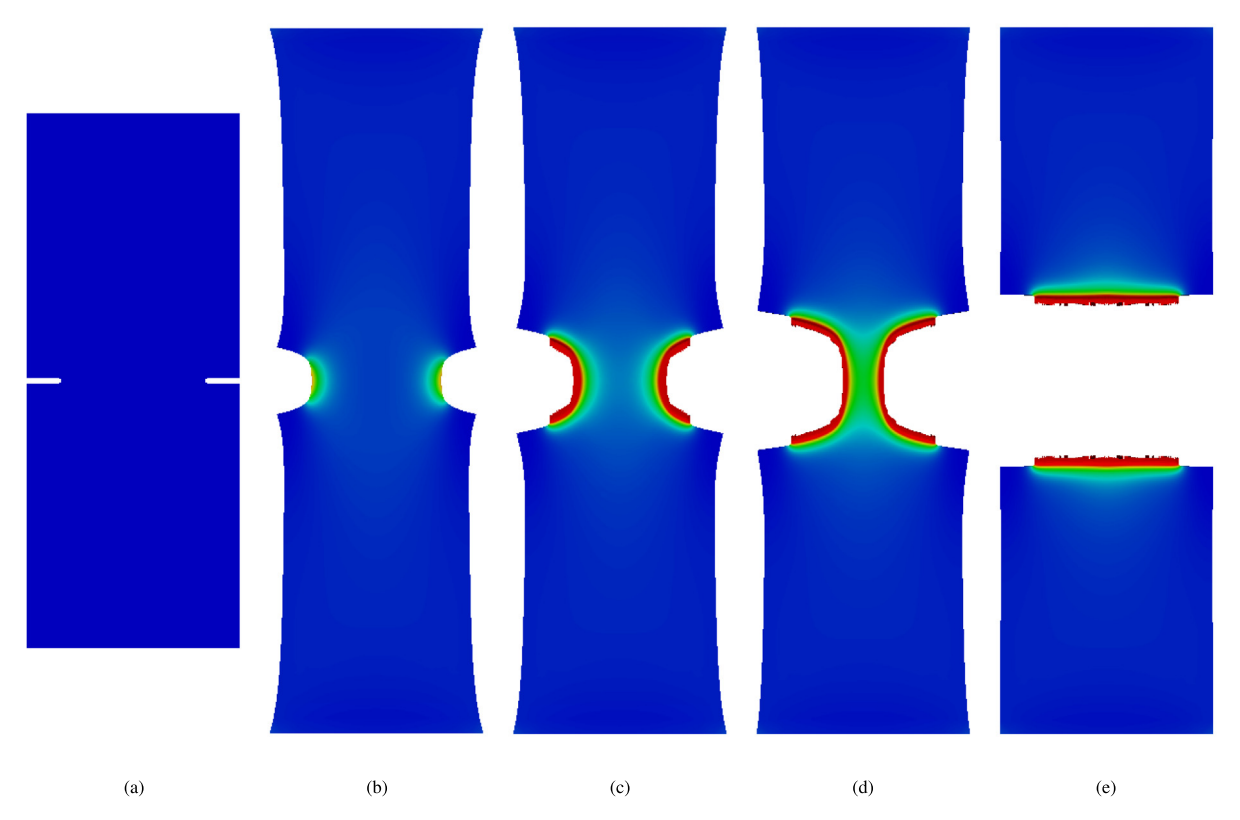


Fig. 6. Visualization of the crack propagation for the case of $a_c = 12$ mm at different stages of the simulation as depicted in Fig. 4(b). The damage contour is illustrated and the regions with d > 0.95 have been removed for the sake of better visualization.

elements do not undergo further out-of-plane contraction, which helps the system's numerical stability. Realistically, as the damaged elements do not have any physical meaning, this can be considered as an acceptable remedy for numerical instabilities. The crack path is visualized at various levels of applied displacement in Fig. 6. The crack can be observed to nucleate at the notch tips and propagate to the center of the specimen.

Using p=2, it is well known that the microsphere network model reduces to the eight-chain model, and this equivalence for even damaged systems is shown in Appendix D with the help of this example. Although the simpler eight-chain network model can be utilized for simulating this example, this simulation is utilized to verify the capability of the current model in estimating the load–displacement behavior and predicting simple crack paths. The current formulation's potential in simulating stable crack propagation using 3D finite elements is also exhibited.

4.2. Rectangular film with rigid inclusions

The crack propagation in a rectangular film made of soft elastomeric TangoBlackPlus material with rigid VeroWhite material circular inclusions has been experimentally studied by Russ et al. [85]. The specimen geometry is as depicted in Fig. 7. The rectangular film has the dimensions $48 \text{ mm} \times 24 \text{ mm} \times 2.5 \text{ mm}$, while the circular inclusions have a diameter of 7.5 mm. The crack lengths a_c considered in the aforementioned study are 5%, 10%, and 20% of the width of the specimen, while the separation distances d_s between the outermost inclusions are chosen to be 18, 24, and 30 mm. Following the convention used in [85] for representing different geometries, the NxxDyy specimen has a crack length a_c of xx% of the width of the specimen and has a separation distance d_s of yy mm. As a modeling assumption, the notch tips are considered to have a very small root radius of R = 0.15 mm. As the behavior of the rigid inclusions is not the main focus of this study, the simpler Neo-Hookean damage model proposed by Miehe and Schänzel [25] is utilized for modeling the behavior of the VeroWhite material. In contrast,

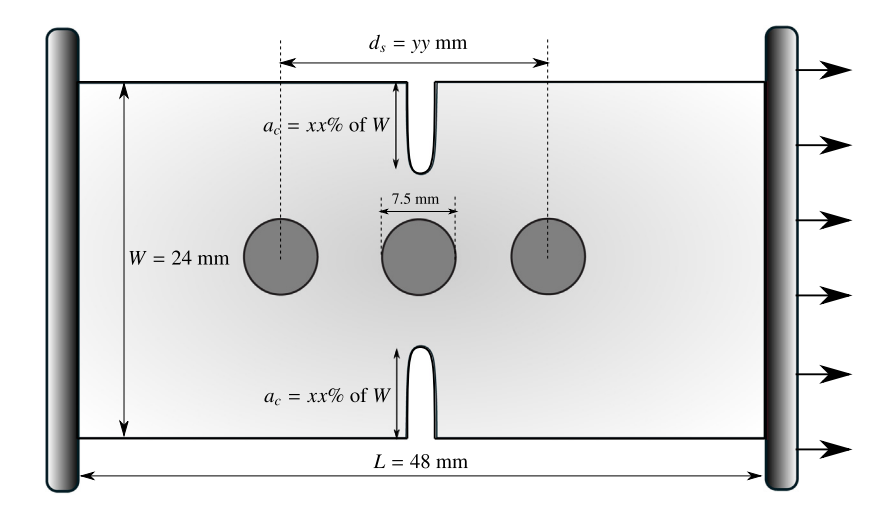


Fig. 7. Geometry of the rectangular film with rigid inclusions specimen represented as NxxDyy.

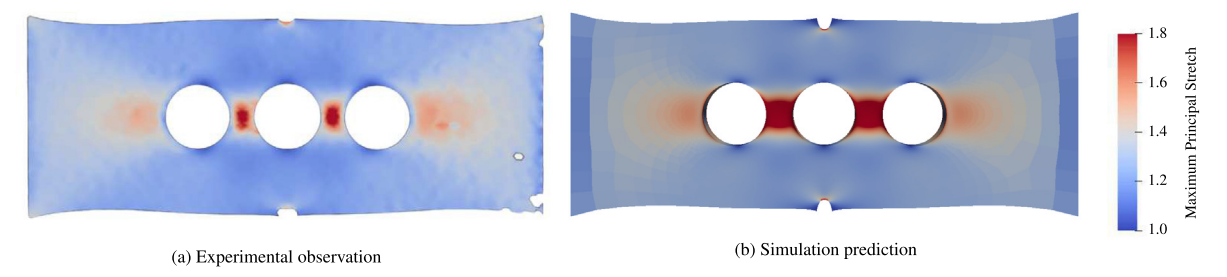


Fig. 8. Comparison of the predicted maximum principal stretch contour with the experimental in-plane stretch distribution for N05D18 specimen at a prescribed end-displacement of 11.8 mm. The rigid inclusions are removed for the sake of better visualization. The figure depicting the experimental stretch distribution obtained using digital image correlation is adapted with permission from [85].

Table 3Parameters used for the soft TangoBlackPlus and the rigid VeroWhite materials in the rectangular film with rigid inclusions specimen.

TangoBlackPlus							VeroWhite			
μ	N	E	p	K	$\bar{arepsilon}_{\mathrm{b}}^{\mathrm{f}}$	ℓ	ζ	$\overline{\mu}$	ν	G_c
0.19 MPa	5.0	50 MPa	2.7	5 MPa	1.6 MPa	0.2 mm	$0.3 \mathrm{s}^{-1}$	714 MPa	0.4	2 N/mm

the current model is used for modeling the elastomer behavior. The calibrated material parameters are tabulated in Table 3.

For the VeroWhite material, the elasticity parameters are chosen following those used in [85]. For the elastomer, a shear modulus of $\mu=0.19$ MPa and a bulk modulus of K=5 MPa, which results in a Poisson's ratio of $\nu=0.481$, are selected during calibration and are along the lines of previously reported parameters for the TangoBlackPlus material [86]. The other polymer material parameters N, E, and p are calibrated based on the prefailure behavior. The parameter ζ is calibrated for capturing the post-peak segment slope of the load-displacement curve, and an appropriate length scale parameter ℓ is also selected, as explained later. The critical rupture energy $\bar{\varepsilon}_b^f$ is approximated based on the critical energy density used in [85], for resulting in similar critical energy release rates based on (33). Depending on this, a much higher value of G_c is approximately chosen for the VeroWhite material. The small positive constant is chosen as $\mathfrak{c}=2\times 10^{-3}$ for ensuring numerical stability of the simulations.

The specimen is subjected to tensile loading at a slow strain rate of 3.5×10^{-3} s⁻¹. While the symmetry about the horizontal axis is assumed in the model, the vertical symmetry is distorted following Russ et al. [85] so that the simulation results match the experimental ones by providing a small perturbation of 0.024 mm to the center inclusion.

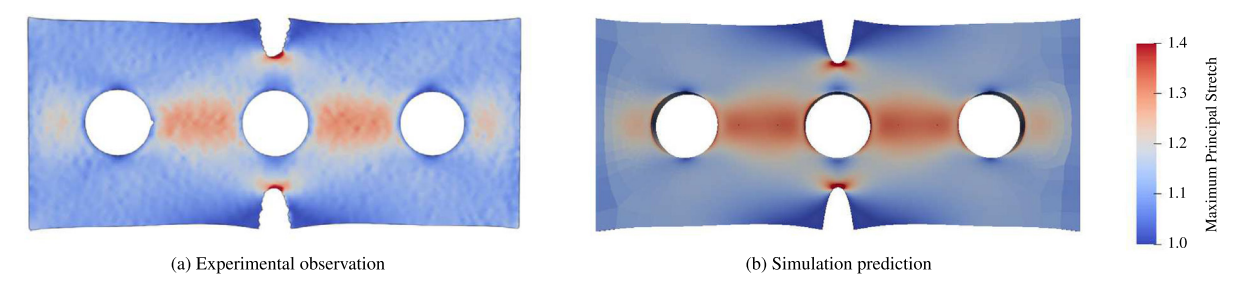


Fig. 9. Comparison of the predicted maximum principal stretch contour with the experimental in-plane stretch distribution for N20D30 specimen at a prescribed end-displacement of 6.6 mm. The rigid inclusions are removed for the sake of better visualization. The figure depicting the experimental stretch distribution obtained using digital image correlation is adapted with permission from [85].

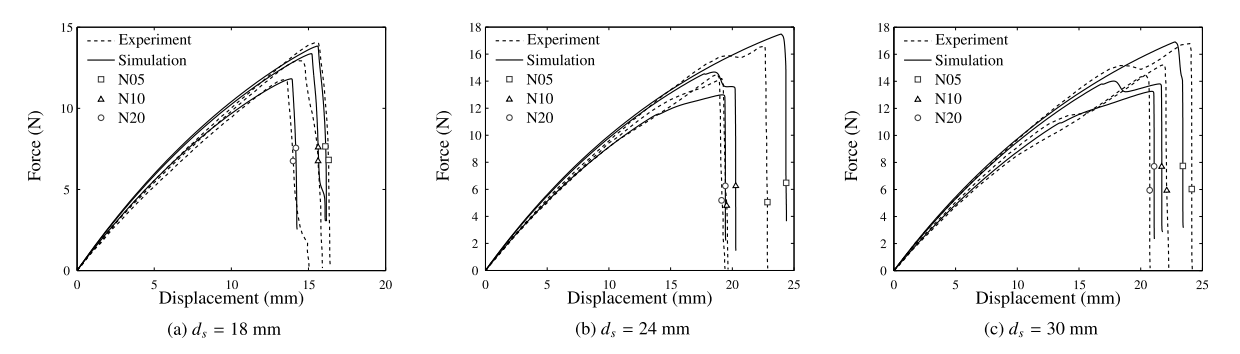


Fig. 10. Load-displacement behavior predicted by the simulations for the rectangular film with rigid inclusions for (a) $d_s = 18$ mm, (b) $d_s = 24$ mm and (c) $d_s = 30$ mm, compared with the experimental data from [85].

Firstly, the predicted maximum principal stretch is compared with the experimental maximum in-plane stretch for verifying the stretch distributions. As it can be observed from Fig. 8, the stretch concentration is more between the rigid inclusions for N05D18 specimen, while the maximum stretch concentration is at the notch tip for N20D30 specimen, as seen in Fig. 9. These also hint at the fracture nucleation regions in these specimens. As the smaller interinclusion distance causes a larger stress concentration, the crack initiates in the region between the inclusions for the N05D18 specimen. However, as the notch tip stress concentration is much larger than that caused by the inclusions, the fracture initiates from the notch tip for the N20D30 specimen. It can also be observed that the predicted maximal principal stretch distributions match reasonably well with the experimental contours. Although the plane stress assumption in [85] predicts the distribution reasonably well, the three-dimensional simulation estimates it slightly better, especially in the region between the inclusions where the crack propagates.

4.2.1. Study of the load-displacement behavior and crack paths

The predicted load-displacement behavior of the specimens is compared with the experimental data reported in [85] for the cases with different notch lengths a_c and inclusion separation distances d_s in Fig. 10. The load-displacement behavior at various stages of crack propagation are visualized for the representative N20D18 and N10D30 specimens in Fig. 11. Furthermore, the crack paths for a few cases are also compared with experimental observations reported in [85], as shown in Figs. 12, 13 and 16. The global stretch values $\bar{\Lambda}$ reported in the above figures are calculated as the ratio of the current length of the specimens to their initial lengths.

As seen in Fig. 11, crack nucleates in the region between the rigid inclusions at the peak load for the N20D18 specimen. As the crack propagates, the reaction force decreases. In the meanwhile, a second crack also initiates at the notch tip, and finally, they combine smoothly, leading to a flat force drop.

For the N10D30 specimen, crack first nucleates at the notch tip. Due to the presence of the rate-dependent damage term and the smaller damage values in the other regions, there is a gradual decrease in the slope of the load-displacement curve. At the same time, the crack proceeds from the notch tip to the center inclusion. This gradual drop is in good agreement with the experimental data, as seen in Fig. 10. As the crack cannot propagate

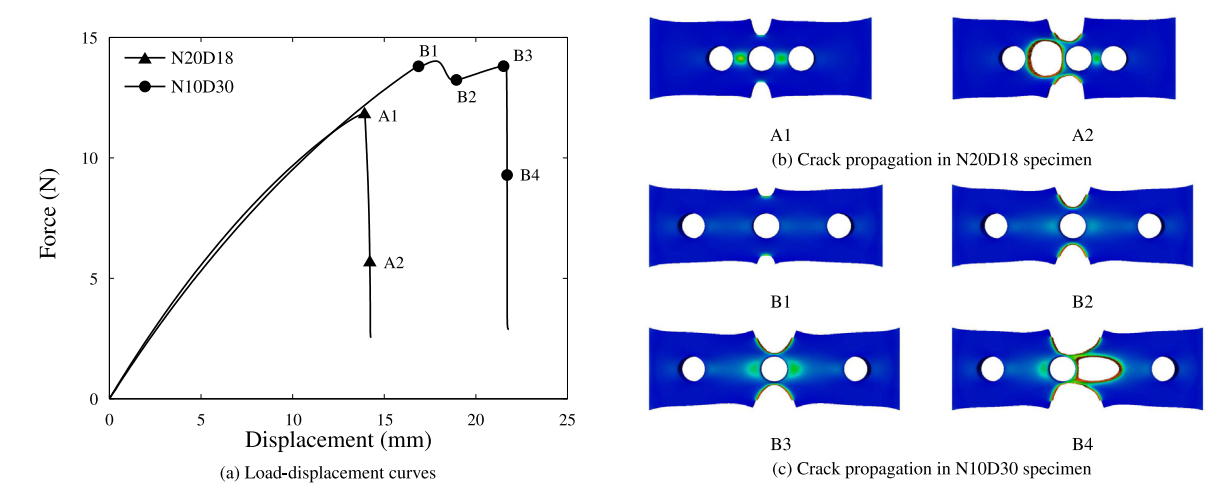


Fig. 11. Depiction of the predicted crack path propagation at different stages of the simulations, following the study by Russ et al. [85]. (a) Simulated load–displacement curves are plotted for the N10D30 and N20D18 specimens, with labels denoting the stages at which the crack paths are depicted. The predicted crack propagation paths are illustrated for (b) N20D18 and (c) N10D30 specimens. The rigid inclusions and the elements with d > 0.95 values are removed for the sake of better visualization.

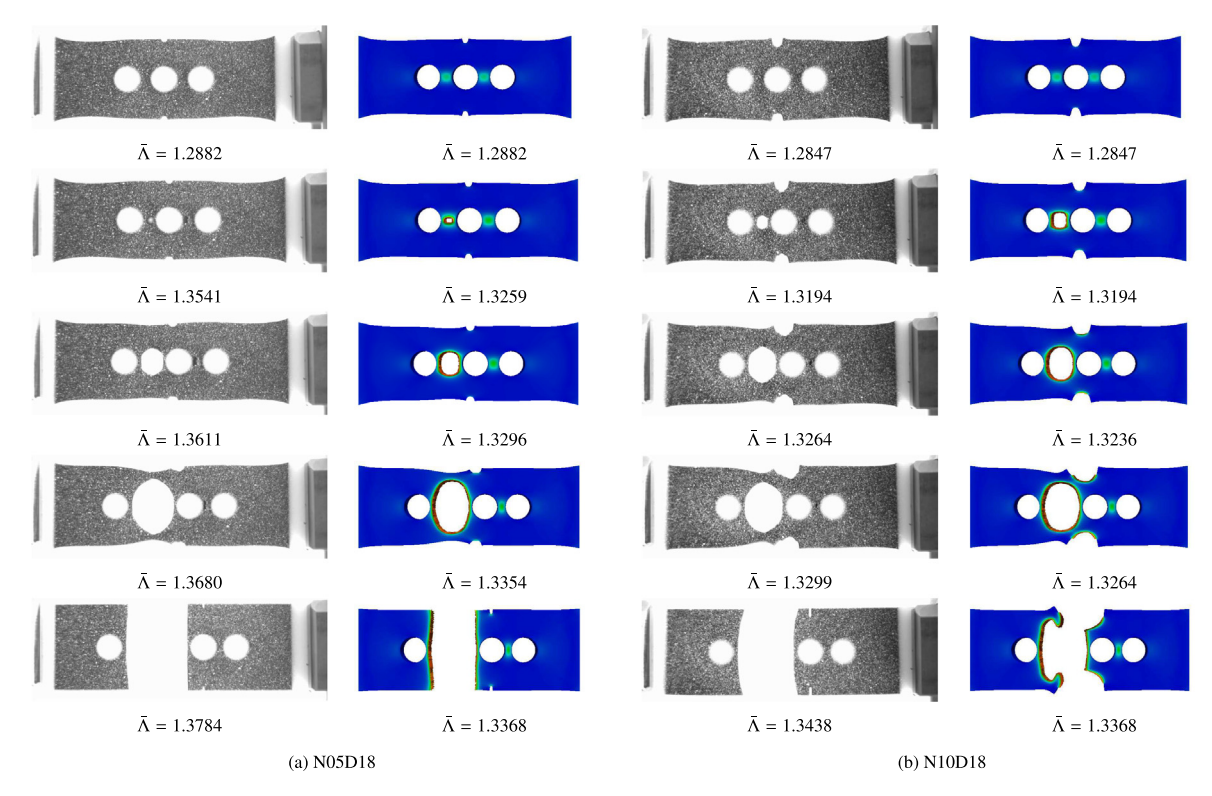


Fig. 12. Comparison of the predicted crack paths at different global stretch values $\bar{\Lambda}$ with experimental data for (a) N05D18 and (b) N10D18 specimens, which have the same inter-inclusion distances, but different initial notch lengths. Source: The experimental images are taken with permission from [85].

further, the specimen in this configuration takes in more load, which is observed in the stiffening segment of its load–displacement curve. A second crack initiates in the region between the inclusions and propagates to join the initial crack. This leads to a sudden decrease in load–displacement behavior.

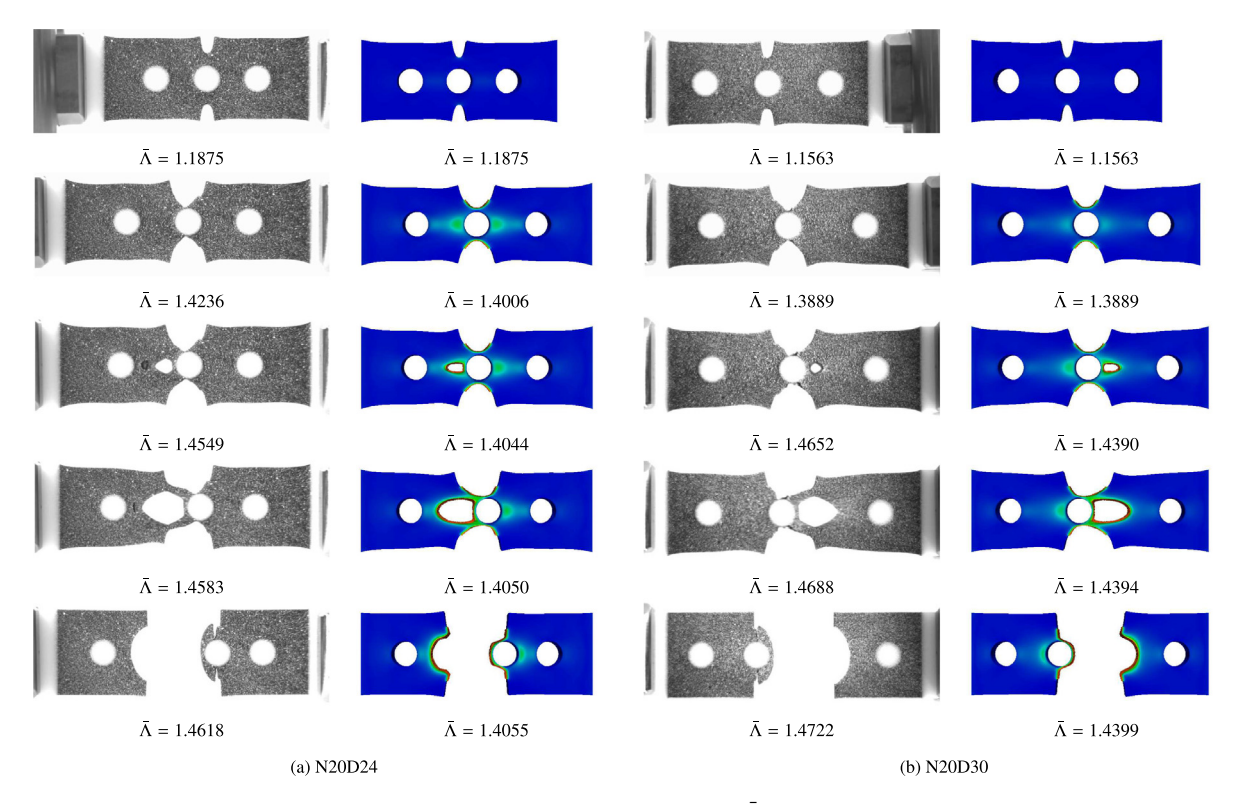


Fig. 13. Comparison of the predicted crack paths at different global stretch values $\bar{\Lambda}$ with experimental data for (a) N20D24 and (b) N20D30 specimens, which have the same initial notch lengths, but different inter-inclusion distances. Source: The experimental images are taken with permission from [85].

As discussed earlier for the N05D18 specimen, the crack nucleates in the region between the inclusions due to higher strain concentration in that region as compared to the notch tip. Once the crack initiates, it propagates through the width of the specimen, as seen in Fig. 12(a). This leads to a force drop, which can be noticed in Fig. 10(a). The model is also able to capture the post-peak segment of the load–displacement curve well. Although the predicted load–displacement behavior and the crack propagation path for the N05D18 specimen match well with the experimental observations, the global stretch values $\bar{\Lambda}$ at which the crack propagation is tracked, do not have an ideal agreement with the corresponding values obtained during simulations. This is also observed in [85], and is attributed to the material's complexity and the fabrication process's inconsistency. Moreover, a slight discrepancy exists between the reported global stretch values and the load–displacement curves in [85]. For example, the global stretch value $\bar{\Lambda}$ reported at crack initiation for the N05D18 specimen is 1.3541, as seen in Fig. 12(a). This corresponds to an applied displacement of 17 mm, while the experimental load–displacement data indicates a complete failure of the specimen at this displacement, as observed in Fig. 10(a). This also contributes to the discrepancies between the predicted and observed global stretch values.

Similar to N05D18, the crack initiation in the N10D18 specimen also takes place in the region between the inclusions. The force drop from the peak load is caused by this crack trying to propagate through the width of the specimen. However, the simulations predict this crack to slow down and finally combine with that emanating from the notch tip, as seen in Fig. 12(b). This results in a small deviation in the post-peak failure segment of the load–displacement curve, as seen in Fig. 10(a). Although the final segment of the crack path slightly deviates from the experimental observations, the model predicts the crack nucleation and its initial propagation well, with even the global stretch values at the different stages being in good agreement.

In the cases with $d_s = 24$ mm, the cracks are found to first initiate from the notch tips. In N05D24, the crack initiates at the notch tip and tries to propagate toward the center inclusion. However, as this occurs at a very high global stretch value and the damage values in the other regions are significant as well, there is a sharper fall in the

reaction force. In the meanwhile, another crack emanates from the region between the inclusions and joins with the former one. Hence, there is a smooth force drop in the load–displacement behavior, as seen in Fig. 10(b).

In the N10D24 specimen, the crack again initiates at the notch tip and propagates till the center inclusion. As this path length is considerably significant, there is an observable initial force drop, which is depicted by Fig. 10(b). Although the specimen is damaged at the notch tip, the applied loading is still insufficient for initiating damage in the region between the inclusions due to the larger inter-inclusion spacing. Hence, the specimen takes in more displacement and a small stiffening segment is visible in Fig. 10(b). It can be noted that the slope of this segment is much lesser due to an increase in the damage in the specimen. However, strain energy accumulates in the region between the inclusions and fracture nucleates there too. The crack emanating from this region finally combines with the crack which originated from the notch tip. This causes the final softening, as observed in Fig. 10(b).

Similar to the N10D24 case, the crack also initiates at the notch tip for the N20D24 specimen. However, due to the large notch length, the amount of material damaged between the notch tip and the center inclusion is much less. Therefore, the slight decrease in the slope of the load–displacement behavior only is observed in Fig. 10(b), which is in good agreement with the experimental observations. Similar to N10D24, the specimen is able to carry more load once the crack originating from the notch tip is arrested by the center inclusion. However, the stiffness is degraded due to damage; hence, the stiffening region's slope is much lesser. Due to the earlier notch tip failure, the strain energy concentration in the region between the inclusions happens quicker than in the N10D24 specimen. Therefore, the N20D24 specimen fails much faster than the N10D24 specimen. Similar to the N10D24 specimen, a secondary crack emanates from the middle region and finally integrates with that starting from the notch tip, as illustrated in Fig. 13(a).

The cases with $d_s = 30$ mm behave similarly to those with $d_s = 24$ mm. For the case of N05D30, although the experimental images show a major crack propagating from only one of the two regions between the inclusions, as seen in Fig. 16, Russ et al. [85] predict cracks emanating on both sides. As illustrated in Fig. 16, this may be due to the choice of a large length scale ℓ value, which helps in the accumulation of damage on both sides. This has been overcome in the current study, and the crack propagation path matches well with the experimental observations.

In summary, although there are slight discrepancies in the predicted load–displacement curves as compared to the experimental data, the overall trends are well captured by the proposed model. Besides, the capability of the proposed model to predict fracture nucleation and complex crack propagation paths in inhomogeneous systems is validated.

Remark 2. The work by Russ et al. [85] considers the damage evolution to initiate when the total free energy exceeds a critical threshold value. As a result, although their model captures the slope of the stiffening regions much better than our work, the failure stretches for cases like N10D30 and N20D30 are predicted to be similar. According to their model, at the point when the cracks originating from the notch tips in N10D30 and N20D30 specimens are arrested by the center inclusion, there would be no damage history in the regions between the inclusions. As a result, both the specimens behave in a similar fashion post this point and hence result in similar failure stretch values. This is overcome by the current model, which considers a continuous damage evolution due to loading, and therefore is capable of distinguishing between the two specimens based on their damage histories at any loading step. As compared to the model proposed by Russ et al. [85], additional traits in the load—displacement behavior are also well captured by the current model due to accounting for the rate-dependent damage term.

4.2.2. Study of the effect of the length scale parameter on the predicted fracture behavior

It is well known that the length scale parameter ℓ is an intrinsic material property [45,58]. For the sake of computational tractability, Talamini et al. [59] proposed to choose the parameter depending on the dimensions of the specimen and to scale the critical bond rupture energy $\bar{\epsilon}_b^f$ so as to retain the order of the product $\bar{\epsilon}_b^f \times \ell \sim G_c$. However, in complex systems wherein there are multiple stress concentration regions, it may be necessary to choose an accurate value of ℓ for better predictions. Therefore, the effect of using different length scale parameters ℓ for simulating the fracture behavior based on experimental data is investigated in this section. In this test, free energy concentrations can occur at the notch tip and in the region between the rigid inclusions. A smaller value of ℓ can better capture the free energy concentration at the notch tip. Still, it would require a higher value of free energy in the regions between the inclusions for fracture initiation. Hence, a suitable length scale parameter ℓ needs to be chosen for balancing the damage effects from these two stress concentration regions in order to improve the accuracy of the predictions.

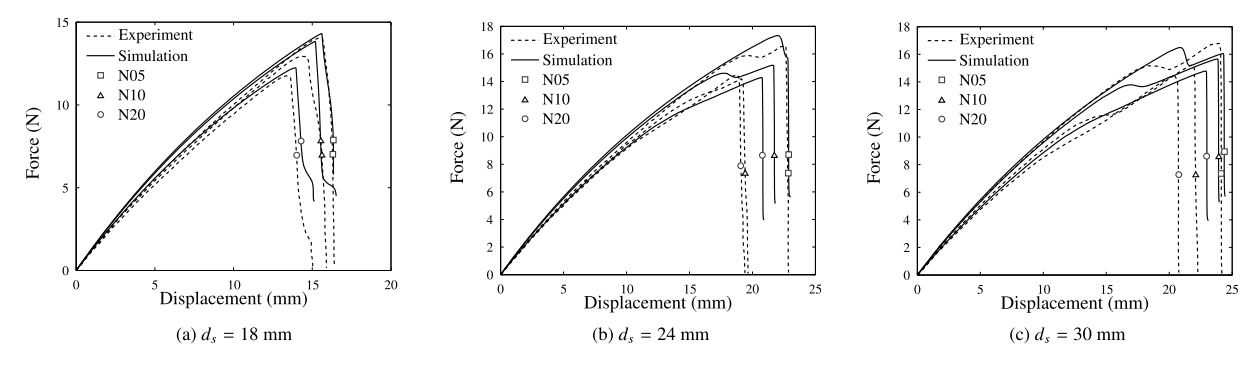


Fig. 14. For studying the effect of the length scale parameter, load-displacement behavior predicted by the simulations using $\ell = 0.1$ mm with $\bar{\epsilon}_b^f = 2.1$ MPa for (a) $d_s = 18$ mm, (b) $d_s = 24$ mm and (c) $d_s = 30$ mm cases, are compared with the experimental data from [85].

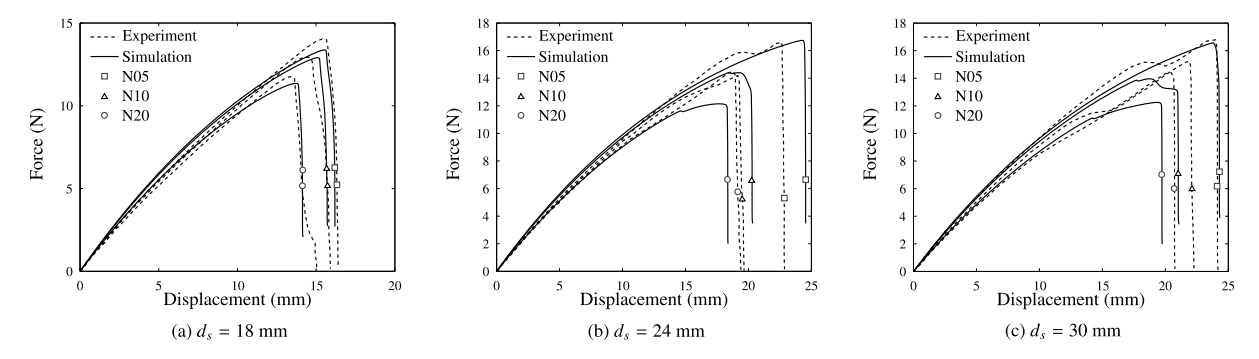


Fig. 15. For studying the effect of the length scale parameter, load-displacement behavior predicted by the simulations using $\ell = 0.3$ mm with $\tilde{\epsilon}_h^{\ell} = 1.25$ MPa for (a) $d_s = 18$ mm, (b) $d_s = 24$ mm and (c) $d_s = 30$ mm cases, are compared with the experimental data from [85].

For this study, all the material parameters tabulated in Table 3 are utilized except for the critical bond rupture energy $\bar{\epsilon}_b^f$, which is calibrated for keeping the load–displacement behavior of N05D18 specimen approximately same for each of the length scale parameters used. With these, the predicted load–displacement behavior for all the cases using $\ell=0.1$ mm and $\ell=0.3$ mm are shown in Figs. 14 and 15 respectively.

For the case of $\ell = 0.1$ mm, the small deviation in the post-peak segment of the load-displacement curve, which is due to the slowing down of the crack emanating in the region between the inclusions, before joining that originating from the notch tip, for the N20D18 specimen is captured. Additionally, the slope of the stiffening segment post the notch tip failure is also better. This stiffening segment in the N05D30 specimen is also captured well. However, the biggest drawback is the incapability of the model to capture the trends in the ultimate failure stretch as obtained from experiments, especially for the cases $d_s = 24$ mm and $d_s = 30$ mm. This can be explained intuitively for the case of $d_s = 30$ mm. It can be observed from Fig. 14(c) that the crack from the notch tip initiates earlier as compared to the cases using larger ℓ . However, as more free energy concentration is required in the region between the inclusions for crack initiation, there are extended stiffening segments for all the specimens, as compared to their counterparts with larger ℓ in Fig. 10(c). Once the crack from the notch tip reaches the center inclusion, the behavior of all three specimens can be expected to be nearly similar, except for the damage histories. As the crack from the notch tip of the N20D30 specimen reaches the center inclusion first, the damage values in the other parts of the specimen can be expected to be higher than those in the other two specimens, and hence it fails first. The other two specimens also follow the same trend and fail at slightly higher global stretch values. However, experimental data shows that the crack from the notch tip of N05D30 specimen originates near the failure stretch of the other two specimens and hence has a much larger ultimate failure stretch. A similar trend can also be observed for the case of $d_s = 24$ mm, which is better captured by using $\ell = 0.2$ mm. However, the crack paths for the N05D30 specimen look similar for the cases using $\ell = 0.1$ mm and $\ell = 0.2$ mm, as seen in Fig. 16.

In contrast, $\ell=0.3$ mm captures the ultimate failure stretch trends much better than the $\ell=0.1$ mm case. However, as the larger length scale value requires smaller free energy concentrations for fracture initiation, cracks

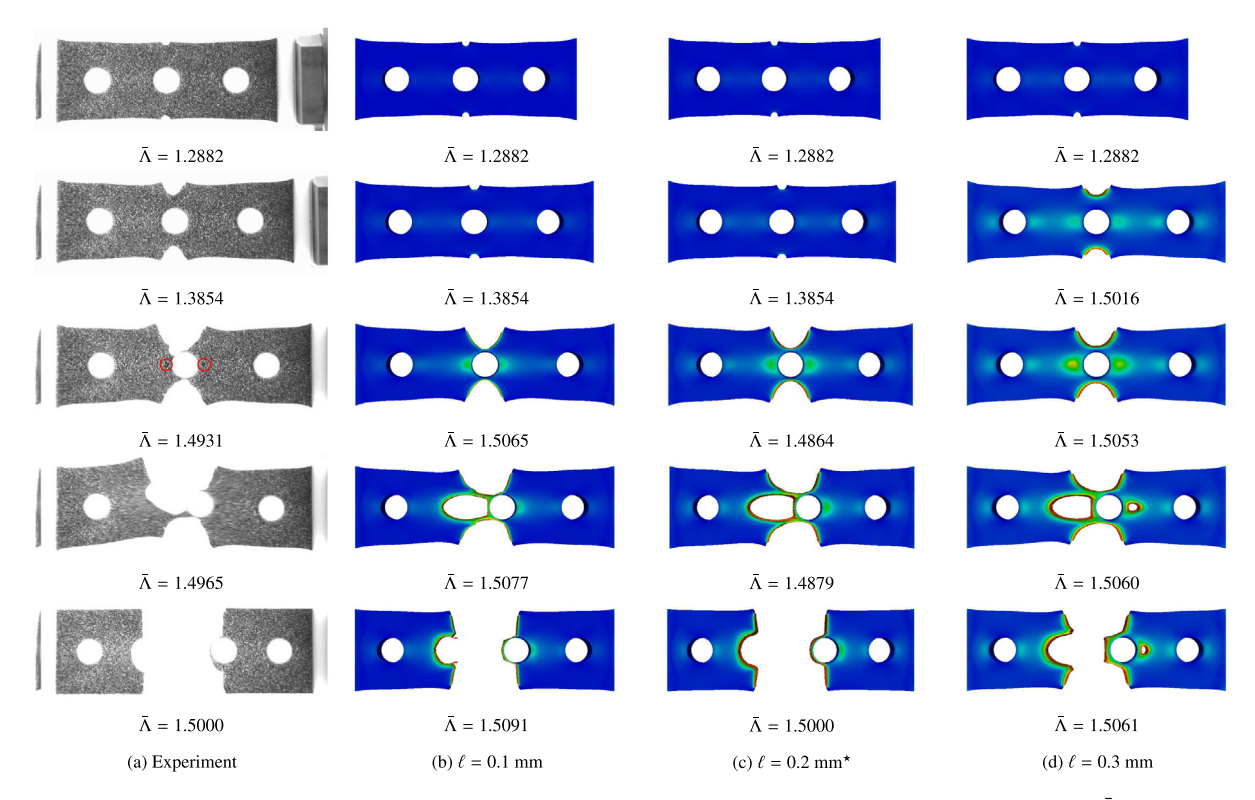


Fig. 16. For studying the effect of length scale parameter ℓ , comparison of the crack paths at different global stretch values $\bar{\Lambda}$ for the N05D30 specimen obtained by (a) experiments, with those predicted by simulations using (b) $\ell = 0.1$ mm with $\bar{\epsilon}_b^f = 2.1$ MPa, (c) $\ell = 0.2$ mm with $\bar{\epsilon}_b^f = 1.6$ MPa and (d) $\ell = 0.3$ mm with $\bar{\epsilon}_b^f = 1.25$ MPa. The value $\ell = 0.2$ mm is chosen in this study. Source: The experimental images are taken with permission from [85].

are found to appear on either side of the center inclusion, as depicted in Fig. 16(d). However, this fact is not evident from the experimental data in Fig. 16(a). Therefore, this high value of the length scale parameter ℓ may not be reasonable.

The crack propagation paths for the N05D18 and N20D30 specimens remain the same irrespective of the length scales used. Besides, the fracture behavior has been found to remain similar for a higher notch radius R = 0.25 mm as well. Additionally, the smaller value of $\bar{\epsilon}_b^f$ chosen for the case of $\ell = 0.3$ mm also does not impact the crack propagation path. These additional findings are reported in Appendix E.

In summary, although the length scale parameter may not play a significant role in accurately predicting the fracture behavior for some specimens like N05D18, it is vital for predicting the accurate trends and crack propagation paths in many cases. This necessitates a proper calibration of this parameter using the experimental data. As a result, more experiments investigating the fracture behavior of elastomers in such complex inhomogeneous systems involving multiple competing stress concentration regions like Russ et al. [85] and Mang et al. [87] are essential for an improved understanding of the physicality and an accurate calibration of the length scale parameter.

5. Conclusions

A multiscale fracture model using the phase field approach has been proposed in this study for computationally estimating the fracture behavior of rubber-like materials. The multiscale elastomer model consists of a microscale polymer chain model, a macroscale continuum model, and a non-affine network model bridging the deformations at the two scales. The microscale damaged chain model assumes that the polymer chains are made up of a number of elastic chain segments, and the damage in the chain is represented by a continuous phase field variable. The total free energy, consisting of the internal energy contribution due to the molecular bond stretching and a free energy component due to the entropy of the chains, is assumed to drive the damage. The role of this

Table A.4Chain parameters used for plotting Fig. 2.

Chain paramete	is used for plotting Fig. 2.	
N	$E_{\rm b}/(k_{\rm B}T)$	$\varepsilon_{\rm b}^{\rm f}/(k_{\rm B}T)$
3	1000	50

assumption in producing a smooth continuous chain response is illustrated. For establishing a relationship between the microscale chain stretch and the macroscopic deformation gradient, the non-affine microsphere model is utilized. However, for integration with the damage model, a new framework is proposed, wherein the minimization of a hypothetical undamaged free energy is considered along with the non-affine constraint. A thermodynamically consistent macroscale model, which is combined with the phase field method, is derived. The total dissipation is assumed to be mainly contributed by molecular bond rupture. Separate history variables for the bulk and chain damage driving energies are introduced and their necessity is discussed. The proposed model is numerically implemented using a monolithic scheme. The standard double-edge notch tensile test is first performed to validate the ability of the model to capture load–displacement behavior and simple crack propagation paths. Furthermore, the tensile test of the rectangular film with rigid inclusions is performed for different notch lengths and inter-inclusion distances. The efficacy of the proposed model in qualitatively estimating complex crack paths and quantitatively predicting the overall fracture behavior in inhomogeneous systems is verified. The necessity of tests involving multiple competing stress concentration regions for enhanced understanding and accurate estimation of the length scale parameter is also illustrated.

In the future, mixed formulations can be developed to extend the applicability of the model to highly incompressible cases. Furthermore, more complex multiscale phenomena like strain-induced crystallization can be augmented with the current formulation for modeling their effects on fracture behavior. Biological applications of the proposed model can also be explored by integrating anisotropy.

Declaration of competing interest

The authors declare that they have no known competing financial interests or personal relationships that could have appeared to influence the work reported in this paper.

Data availability

Data will be made available on request.

Acknowledgments

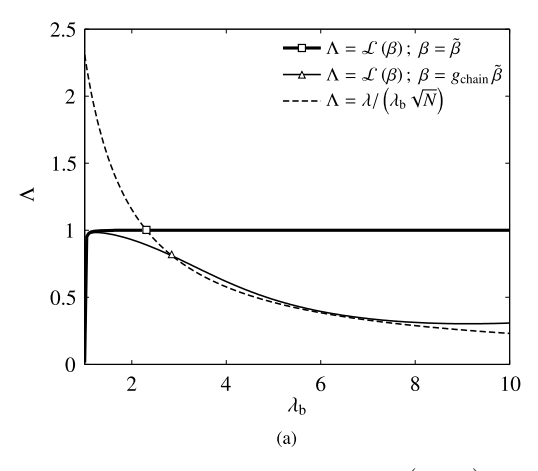
Financial support for this research was provided by the Department of Energy, National Nuclear Security Administration, USA, Predictive Science Academic Alliance Program (PSAAP), USA under Award Number DE-NA0003962, and the National Science Foundation, USA through grant CMMI-1911836. This support is gratefully acknowledged.

Appendix A. Additional details and explanations of the chain response

The chain response using the microscale damaged chain model proposed in this study has been visualized in Section 2.1 and compared with alternate formulations commonly used in literature. The equations tabulated in Table 1, along with Eqs. (1), (3), (4), (5), (6), (8) and (13), are used for plotting Fig. 2.

The values of the parameters used are in line with those used in [59] and are tabulated in Table A.4. However, it must be noted that the value of $\varepsilon_b^f/(k_BT)$ is halved in order to mimic a similar response as that obtained in the aforementioned study.

For Model 1, which assumes $\psi_d = g_{\text{chain}} \psi_{\text{bond}} + \psi_{\text{ent}}$, there is an observable discontinuity in the chain response as seen in Fig. 2 at an applied stretch of $\bar{\lambda} = 4.12$. In order to visualize the reason for such a jump, plots of Λ vs λ_b are produced at two applied stretches $\bar{\lambda} = 4.0$ and $\bar{\lambda} = 4.3$ as shown in Fig. A.17. Further, the above formulation is compared with the current model in order to illustrate how the issue is overcome.



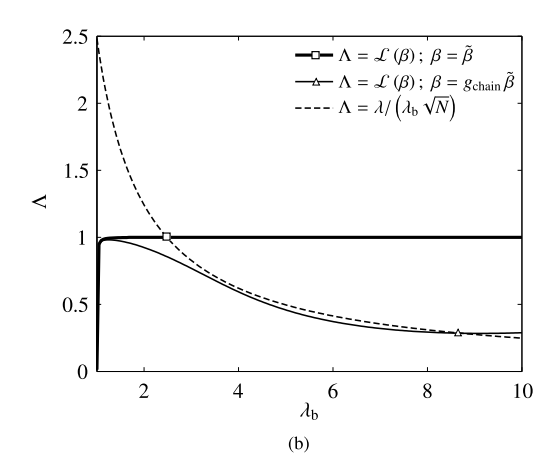


Fig. A.17. Illustration of $\Lambda = \mathcal{L}(\beta)$ and $\Lambda = \lambda/\left(\lambda_b\sqrt{N}\right)$, which are the LHS and RHS of (A.1) at applied stretches of (a) $\bar{\lambda} = 4.0$ and (b) $\bar{\lambda} = 4.3$. The current model, wherein the degradation of the total free energy is assumed and thus $\beta = \tilde{\beta}$, is compared with Model 1, which considers the degradation of only the bond stretch energy, thus leading to $\beta = g_{\text{chain}}\tilde{\beta}$. The expression for $\tilde{\beta}$ is given by (A.2).

At any given applied stretch $\bar{\lambda}$, the magnitude of the bond stretch λ_b can be obtained as the minimizer of the total damaged free energy using (10). One method for solving the resulting nonlinear equation is to consider the expressions of Langevin parameter Λ obtained from its physical perspective and the Langevin statistics. From its physical meaning, it can be expressed as $\Lambda = \lambda/\left(\lambda_b\sqrt{N}\right)$, while it is given by $\Lambda = \mathcal{L}\left(\beta\right)$ using the Langevin statistics. The expression for β can be obtained from the aforementioned minimization problem. If the plots of these two expressions of Λ are produced for different values of λ_b , the point of their intersection results in the root of the nonlinear equation. This method has been used in Fig. A.17 in order to find the value of λ_b at the two applied stretches. So, the equation used for solving λ_b can be written as

$$\underbrace{\mathcal{L}(\beta)}_{\text{LHS}} = \underbrace{\lambda / \left(\lambda_{\text{b}} \sqrt{N}\right)}_{\text{DVS}}.$$
(A.1)

The value of β for the two formulations can be obtained from Table 1. For simplifying the notation, we assume $\tilde{\beta}$ as

$$\tilde{\beta} := \frac{E_{\rm b}\sqrt{N}}{k_{\rm B}T} \frac{\lambda_{\rm b}^2 (\lambda_{\rm b} - 1)}{\lambda} \,. \tag{A.2}$$

As the value of β degrades with damage for Model 1, which considers $\psi_d = g_{\text{chain}}\psi_{\text{bond}} + \psi_{\text{ent}}$, the value of λ_b obtained as the root of the equation at the two applied stretches has a large jump, which is overcome by the current model.

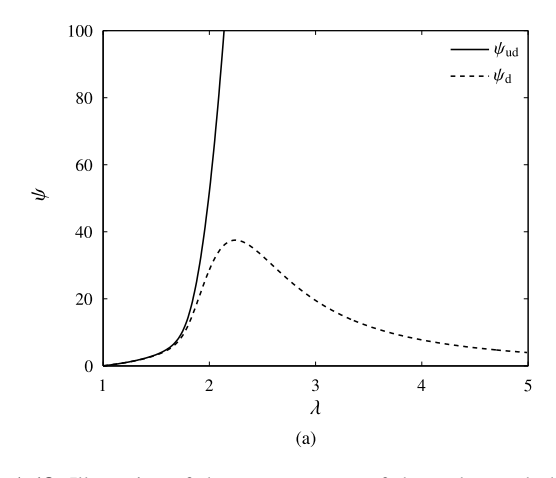
Further, for the utilization of the current model with the microsphere network model, the plots of the damaged and undamaged chain-free energies and their slopes are depicted in Fig. A.18. The same set of parameters in Table A.4 is used for plotting these curves. The convex nature of the undamaged free energy function and the general non-convex nature of the damaged free energy function are visible.

Appendix B. Derivation of macroscale constitutive equations

As rubber-like materials are known for their high stretchability, the constitutive framework is developed in the finite deformation regime. The subsequent sections introduce the kinematics and derive the governing equations using the balance laws, and are based on the frameworks described in [32,59,71,88–90].

B.1. Finite strain kinematics

A body is considered to be a collection of material points, which occupy the spatial configuration $V \subset \mathbb{R}^{n_{\text{dim}}}$, with $1 \le n_{\text{dim}} \le 3$ representing the spatial dimension, at time $t \in \mathbb{R}_+$. The position of an individual material point



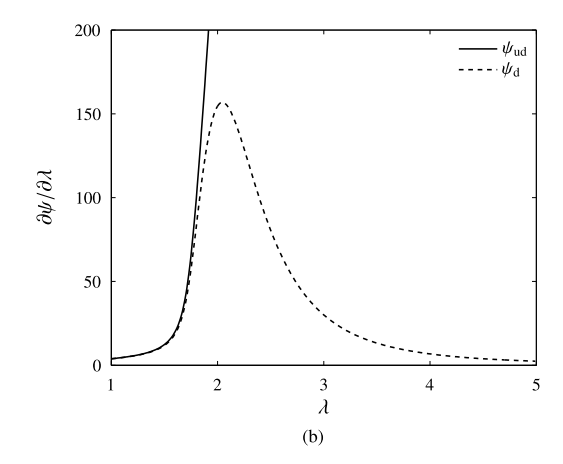


Fig. A.18. Illustration of the convex nature of the undamaged chain free energy ψ_{ud} and the non-convex behavior of the damaged chain free energy ψ_{d} with respect to the stretch λ in the chain. (a) Free energy functions and (b) their slopes are plotted.

is given by $x \in V$, while the boundary is denoted by $A \subset \mathbb{R}^{n_{\text{dim}}-1}$. The displacements of these points due to the deformation of the body are described relative to a fixed reference configuration $V_0 \subset \mathbb{R}^{n_{\text{dim}}}$, which for instance, can be the configuration occupied by the body at time t_0 . At this time, the position of the material point is given by $X \in V_0$, while the boundary is denoted by $A_0 \subset \mathbb{R}^{n_{\text{dim}}-1}$.

A nonlinear deformation map $\varphi(X): X \mapsto x = \varphi(X;t)$ is utilized to map the reference positions $X \in V_0$ onto the current positions $x \in V$. The local deformation gradient $F = \nabla_X \varphi(X;t)$ represents the linear mapping of the tangent vectors between the reference and spatial configurations. The Jacobian $J = \det F > 0$ represents the ratio of the current local volume to its initial volume. The spatial velocity gradient I and the rate of deformation tensor I are defined as

$$\mathbf{l} = \dot{\mathbf{F}}\mathbf{F}^{-1}$$
 $\mathbf{D} = \operatorname{sym}\mathbf{l} = \frac{1}{2}(\mathbf{l} + \mathbf{l}^T)$. (B.1)

The displacement field of any point is given by u = x - X. The damage at any point in the continuum is represented using a continuous phase field variable $d(X,t) \in [0,1]$. At any point, d=0 denotes a fully intact material, while d=1 indicates a fully fractured material. Further, the irreversibility of the microstructural changes leading to fracture is taken into account by assuming the damage variable to grow monotonically $\dot{d}(X,t) \geq 0$. Additionally, the dimensionless positive-valued internal variable $\lambda_b > 0$ is used as the macroscopic variable for tracking chain bond stretch.

As the microsphere model predicts an isotropic network response, all the chains at a material point have the same properties. In addition, we assume that the continuum damage is mainly due to the rupture of the molecular bonds in the monomers. This makes it reasonable to approximate the continuum damage with the microscale chain damage, which is caused due to the molecular bond rupture. Hence, in this study, the chain damage is also denoted by the same variable d. Similarly, the chain bond stretch is also denoted by λ_b , which is the same as the non-physical macroscopic variable used for tracking it.

B.2. Balance laws

The constitutive relations are derived based on the macro-forces and micro-forces balance laws and the laws of thermodynamics. The subsequent formulation is derived in the reference configuration, though a similar derivation can also be performed in the spatial configuration.

Balance of mass. Assuming the conservation of mass of the system at all times, the local form of the balance of mass in the reference configuration is given by

$$\dot{\rho}_0 = 0 \quad \text{in } V_0 \,, \tag{B.2}$$

wherein ρ_0 represents the mass density per unit reference volume.

Balance of linear momentum. By equating the rate of linear macro-momentum to the mechanical macro-forces, the balance law in the reference configuration can be written as

$$\frac{\mathrm{d}}{\mathrm{d}t} \int_{V_0} \rho_0 \dot{\boldsymbol{u}} \, \mathrm{d}V_0 = \int_{V_0} \boldsymbol{B} \, \mathrm{d}V_0 + \int_{A_0} \boldsymbol{P} \boldsymbol{N} \, \mathrm{d}A_0 \quad \to \quad \text{Div } \boldsymbol{P} + \boldsymbol{B} = \rho_0 \ddot{\boldsymbol{u}} \quad \text{in } V_0 \,, \tag{B.3}$$

wherein B represents the body force per unit reference volume, P is the first Piola-Kirchhoff stress tensor and N denotes the outward normal at the boundary in the reference configuration. The term $\rho_0 \dot{u}$ represents the macro-momentum at a given point.

Balance of angular momentum. The balance of angular momentum in the reference configuration can be written as

$$\frac{\mathrm{d}}{\mathrm{d}t} \int_{V_0} \boldsymbol{X} \times \rho_0 \dot{\boldsymbol{u}} \, \mathrm{d}V_0 = \int_{V_0} \boldsymbol{X} \times \boldsymbol{B} \, \mathrm{d}V_0 + \int_{A_0} \boldsymbol{X} \times \boldsymbol{P} \boldsymbol{N} \, \mathrm{d}A_0 \quad \rightarrow \quad \boldsymbol{P} \boldsymbol{F}^T = \boldsymbol{F} \boldsymbol{P}^T \quad \text{in } V_0 \, . \tag{B.4}$$

Balance of micro-forces. Due to the damage variable d, assuming that the stress level in the microscopic system is characterized by an intrinsic micro-force $\pi_d(X, t)$, an extrinsic micro-force $h_d(X, t)$ and a micro-stress vector $\boldsymbol{\xi}_d(X, t)$, the balance of the micro-forces due to the damage field can be written as

$$\frac{\mathrm{d}}{\mathrm{d}t} \int_{V_0} \rho_0 \mathcal{A}_{\mathrm{d}} \dot{d} \, \mathrm{d}V_0 = \int_{V_0} h_{\mathrm{d}} \, \mathrm{d}V_0 + \int_{V_0} \pi_{\mathrm{d}} \, \mathrm{d}V_0 + \int_{A_0} \xi_{\mathrm{d}} \cdot N \, \mathrm{d}A_0 \quad \to \quad \text{Div } \xi_{\mathrm{d}} + h_{\mathrm{d}} + \pi_{\mathrm{d}} = \rho_0 \mathcal{A}_{\mathrm{d}} \ddot{d} \quad \text{in } V_0 \,, \quad (B.5)$$

wherein \mathcal{A}_d represents the micro-inertia for damage and $\rho_0 \mathcal{A}_d \dot{d}$ denotes the micro-momentum due to damage at any given point. Note that the micro-inertia is assumed as time-independent. Defining similar counterparts for the bond stretch variable λ_b , the corresponding micro-force balance can be written as

$$\frac{\mathrm{d}}{\mathrm{d}t} \int_{V_0} \rho_0 \mathcal{A}_b \dot{\lambda}_b \, \mathrm{d}V_0 = \int_{V_0} h_b \, \mathrm{d}V_0 + \int_{V_0} \pi_b \, \mathrm{d}V_0 \quad \rightarrow \quad h_b + \pi_b = \rho_0 \mathcal{A}_b \ddot{\lambda}_b \quad \text{in } V_0 \,. \tag{B.6}$$

As the bond stretch is defined as an internal variable without nonlocal effects, it is assumed that it is not associated with a micro-stress, which is reflected in the above equation.

First law of thermodynamics. The total energy balance of the system can be expressed as

$$\frac{\mathrm{d}}{\mathrm{d}t} \int_{V_0} (\rho_0 e_0 + K_0) \, \mathrm{d}V_0 = \int_{V_0} \left(\mathbf{B} \cdot \dot{\mathbf{u}} + h_{\mathrm{d}} \dot{d} + h_{\mathrm{b}} \dot{\lambda}_{\mathrm{b}} + \rho_0 r_0 \right) \, \mathrm{d}V_0 + \int_{A_0} \left(\mathbf{P} \mathbf{N} \cdot \dot{\mathbf{u}} + \boldsymbol{\xi}_{\mathrm{d}} \cdot \mathbf{N} \dot{d} - \boldsymbol{q}_0 \cdot \mathbf{N} \right) \, \mathrm{d}A_0 \,, \tag{B.7}$$

wherein e_0 represents the internal energy per unit reference mass, r_0 is the heat source per unit reference mass and q_0 denotes the referential heat flux vector. The kinetic energy in the reference configuration K_0 can be expressed as

$$K_0 = \frac{1}{2}\rho_0\dot{\boldsymbol{u}}\cdot\dot{\boldsymbol{u}} + \frac{1}{2}\rho_0\mathcal{A}_d\left(\dot{d}\right)^2 + \frac{1}{2}\rho_0\mathcal{A}_b\left(\dot{\lambda}_b\right)^2. \tag{B.8}$$

Utilizing all the above results, the equation for the first law of thermodynamics can be simplified to the local form

$$\rho_0 \dot{e}_0 = \mathbf{P} : \dot{\mathbf{F}} + \boldsymbol{\xi}_{d} \cdot \nabla_{\mathbf{X}} \dot{d} - \pi_{d} \dot{d} - \pi_{b} \dot{\lambda}_{b} + \rho_0 r_0 - \text{Div } \boldsymbol{q}_0 \quad \text{in } V_0.$$
(B.9)

Second law of thermodynamics. The second law of thermodynamics can be expressed as

$$\frac{\mathrm{d}}{\mathrm{d}t} \int_{V_0} \rho_0 s_0 \, \mathrm{d}V_0 \ge \int_{V_0} \frac{\rho_0 r_0}{T} \, \mathrm{d}V_0 - \int_{A_0} \frac{\mathbf{q}_0 \cdot \mathbf{N}}{T} \, \mathrm{d}A_0 \,, \tag{B.10}$$

with T representing the absolute temperature of the system and s_0 denoting the referential entropy per unit mass. This equation can be simplified to the local form as

$$\rho_0 \dot{s}_0 T \ge \rho_0 r_0 - \text{Div } \boldsymbol{q}_0 + \frac{\boldsymbol{q}_0 \cdot \nabla_X T}{T} \quad \text{in } V_0.$$
(B.11)

The Helmholtz free energy function ψ is introduced using the Legendre-transformation

$$e_0 := \psi + Ts_0. \tag{B.12}$$

Using Eqs. (B.9), (B.11) and (B.12), we get

$$\mathbf{P}: \dot{\mathbf{F}} + \boldsymbol{\xi}_{\mathrm{d}} \cdot \nabla_{\mathbf{X}} \dot{d} - \pi_{\mathrm{d}} \dot{d} - \pi_{\mathrm{b}} \dot{\lambda}_{\mathrm{b}} - \rho_{0} \dot{\psi} - \rho_{0} s_{0} \dot{T} - \frac{\boldsymbol{q}_{0} \cdot \nabla_{\mathbf{X}} T}{T} \ge 0. \tag{B.13}$$

For this study, a quasi-static loading condition is assumed; hence, the inertial effects are neglected. The external body macro-force B and micro-forces h_d , h_b are also neglected. Further, an isothermal process with a uniform temperature distribution is assumed; therefore, \dot{T} , $\nabla_X T$ are approximated as zero. Let $\Psi = \rho_0 \psi$ and the stresses are expressed in terms of the symmetric Kirchhoff stress tensor $\tau = PF^T$. Using these assumptions and conventions, the Eqs. (35), (36), (37) and (38) are obtained.

Appendix C. History variables for damage driving fields

As the macroscopic free energy is split into volumetric and isochoric responses, and different degradation functions are used, the necessity and validity of the history variables for both the damage driving fields need to be studied. Following the study presented in [80], we consider a local damage model in a one-dimensional setting. Although we do not explicitly use the expressions for U_{bulk} and $\bar{\psi}_{\text{ud}}$, their convex nature with respect to the applied loading is utilized. Let us consider the free energy function as

$$\Psi = g_{\text{bulk}} U_{\text{bulk}} + g_{\text{chain}} \bar{\psi}_{\text{ud}}, \tag{C.1}$$

with the cubic and quadratic forms of the g_{bulk} and g_{chain} degradation functions, respectively, as used in the current study. Using the second law of thermodynamics, the reduced dissipation inequality is given by

$$\mathcal{D} = f_{\rm d}\dot{d} \ge 0 \quad \text{with} \quad f_{\rm d} = -\frac{\partial \Psi}{\partial d} = 3(1-d)^2 U_{\rm bulk} + 2(1-d) \bar{\psi}_{\rm ud} \,. \tag{C.2}$$

Similar to the threshold functional presented in [80], assuming the crack resistance force to be linear in damage, as used in the current study, we get

$$f_{\rm d} = \mathfrak{f}d \quad \to \quad d = \frac{\left(6U_{\rm bulk} + 2\bar{\psi}_{\rm ud} + \mathfrak{f}\right) - \sqrt{\left(2\bar{\psi}_{\rm ud} + \mathfrak{f}\right)^2 + 12U_{\rm bulk}\mathfrak{f}}}{6U_{\rm bulk}} \,. \tag{C.3}$$

Note that f is assumed to be a positive constant. Assuming damage to occur mainly in tension, both U_{bulk} and $\bar{\psi}_{\text{ud}}$ are positive. Hence, the other root of the above equation is discarded as it results in d > 1. Except for the point $U_{\text{bulk}} = 0$, the damage field is defined everywhere. At very small loadings, we have

$$U_{\rm bulk} \sim \bar{\psi}_{\rm ud} \sim \epsilon \to 0 \longrightarrow d \approx \frac{\mathfrak{f} - \mathfrak{f}}{6\epsilon} \approx 0.$$
 (C.4)

At very large loadings, three cases can be possible.

$$U_{\text{bulk}} \sim \bar{\psi}_{\text{ud}} \sim \epsilon \to \infty \longrightarrow d \approx \frac{(6+2+\mathfrak{f}/\epsilon) - \sqrt{(2+\mathfrak{f}/\epsilon)^2 + 12\mathfrak{f}/\epsilon}}{6} \approx 1.$$
 (C.5)

$$U_{\rm bulk} \ll \bar{\psi}_{\rm ud} \sim \epsilon \to \infty \longrightarrow d \approx \frac{(6U_{\rm bulk} + 2\epsilon + \mathfrak{f}) - (2\epsilon + \mathfrak{f})}{6U_{\rm bulk}} \approx 1.$$
 (C.6)

$$\bar{\psi}_{\rm ud} \ll U_{\rm bulk} \sim \epsilon \to \infty \longrightarrow d \approx \frac{\left(6 + 2\bar{\psi}_{\rm ud}/\epsilon + \mathfrak{f}/\epsilon\right) - \sqrt{\left(2\bar{\psi}_{\rm ud}/\epsilon + \mathfrak{f}/\epsilon\right)^2 + 12\mathfrak{f}/\epsilon}}{6} \approx 1.$$
 (C.7)

Further, the partial derivatives of the damage variable with respect to the damage driving fields can be derived and simplified as

$$\frac{\partial d}{\partial \bar{\psi}_{\rm ud}} = \frac{g - \left(2\bar{\psi}_{\rm ud} + \mathfrak{f}\right)}{3U_{\rm bulk}g} > 0 \quad \text{with} \quad g = \sqrt{\left(2\bar{\psi}_{\rm ud} + \mathfrak{f}\right)^2 + 12U_{\rm bulk}\mathfrak{f}}.$$
 (C.8)

$$\frac{\partial d}{\partial U_{\text{bulk}}} = \frac{6\mathfrak{f}^2}{g\left[\left(\left(2\bar{\psi}_{\text{ud}} + \mathfrak{f}\right)^2 + 6U_{\text{bulk}}\mathfrak{f}\right) + \left(2\bar{\psi}_{\text{ud}} + \mathfrak{f}\right)g\right]} > 0.$$
 (C.9)

First, the damage variable has been shown to converge to zero at smaller loadings, and to one at very large loadings, thus validating the choice of the degradation functions. Further, it has been proven that the damage variable

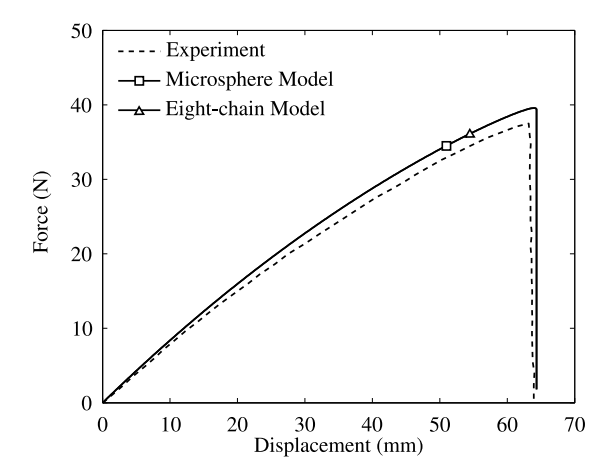


Fig. D.19. Comparison of the simulation results using microsphere model with p=2 and eight-chain model, using the same set of parameters, with the experimental data from [15] for a double-edge notched specimen with $a_c=12$ mm.

is an increasing function concerning each damage driving field. Therefore, decreasing damage driving fields strictly lead to a decrease in the damage variable.

As an example case, during the compressive part of the cyclic loading, both the damage driving fields tend to decrease. For satisfying irreversibility of the damage $\dot{d} \geq 0$, both the functions need to be non-decreasing, and hence history variables are required for both the functions. Therefore, for a general model, history variables are required for each of the damage driving fields and it has been proven that they ensure damage irreversibility $\dot{d} > 0$.

Appendix D. Double-edge notch tensile specimen - Comparison with eight-chain model

The current formulation using the generalized microsphere model as the bridge linking the deformations at the two scales can be shown to be equivalent to that using the eight-chain model when p = 2. For this sake, the alternate formulation, wherein the eight-chain network model is used, is implemented in a similar manner with the mapping between the chain stretch and the isochoric deformation gradient given by [49,91]

$$\lambda = \sqrt{\frac{\text{tr}\bar{C}}{3}} \quad \text{with} \quad \bar{C} = \bar{F}^T \bar{F} . \tag{D.1}$$

With this model, the double-edge notch tensile test is simulated for the specimen with $a_c = 12$ mm using the same set of material parameters as tabulated in Table 2. The resulting load-displacement behavior is compared with that obtained using the microsphere network model, as shown in Fig. D.19. It can be observed that the results match perfectly, thus verifying the equivalence.

Appendix E. Rectangular film with rigid inclusions - Additional details and results

A custom mesh, as depicted in Fig. E.20, is generated with the most refined regions having an element size of 0.03 mm. For the N20D30 specimen, this mesh results in 4.23 million degrees of freedom.

To study the effect of the length scale parameter ℓ on accurately predicting the fracture behavior, the crack propagation paths using $\ell=0.1$ mm, $\ell=0.2$ mm, and $\ell=0.3$ mm are compared with the experimental data for the N05D18 and N20D30 specimens in Figs. E.21 and E.22, respectively. It can be observed that the length scale parameter has a negligible effect on the crack propagation path for the N05D18 specimen. It is observed that a small value of ℓ predicts additional cracks between those emanating from the notch tip and the region between the inclusions, as seen in Fig. E.22(b) at a global stretch of $\bar{\Lambda}=1.4790$. However, this is quite insignificant, and

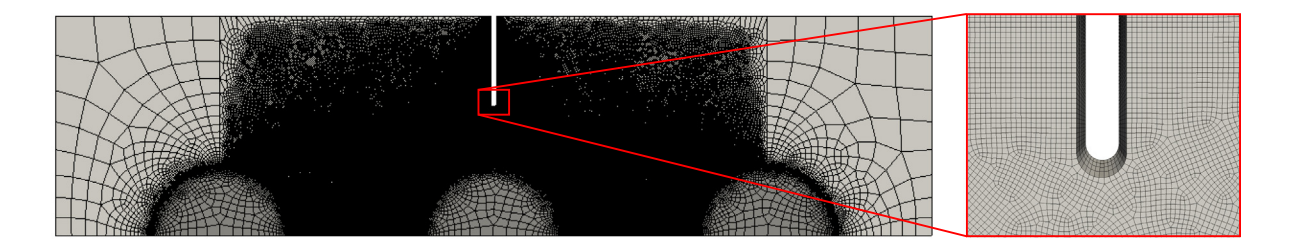


Fig. E.20. N20D30 specimen mesh used for the simulation of the rectangular film with rigid inclusions tensile test. Symmetry is utilized for modeling just one-fourth of the whole specimen.

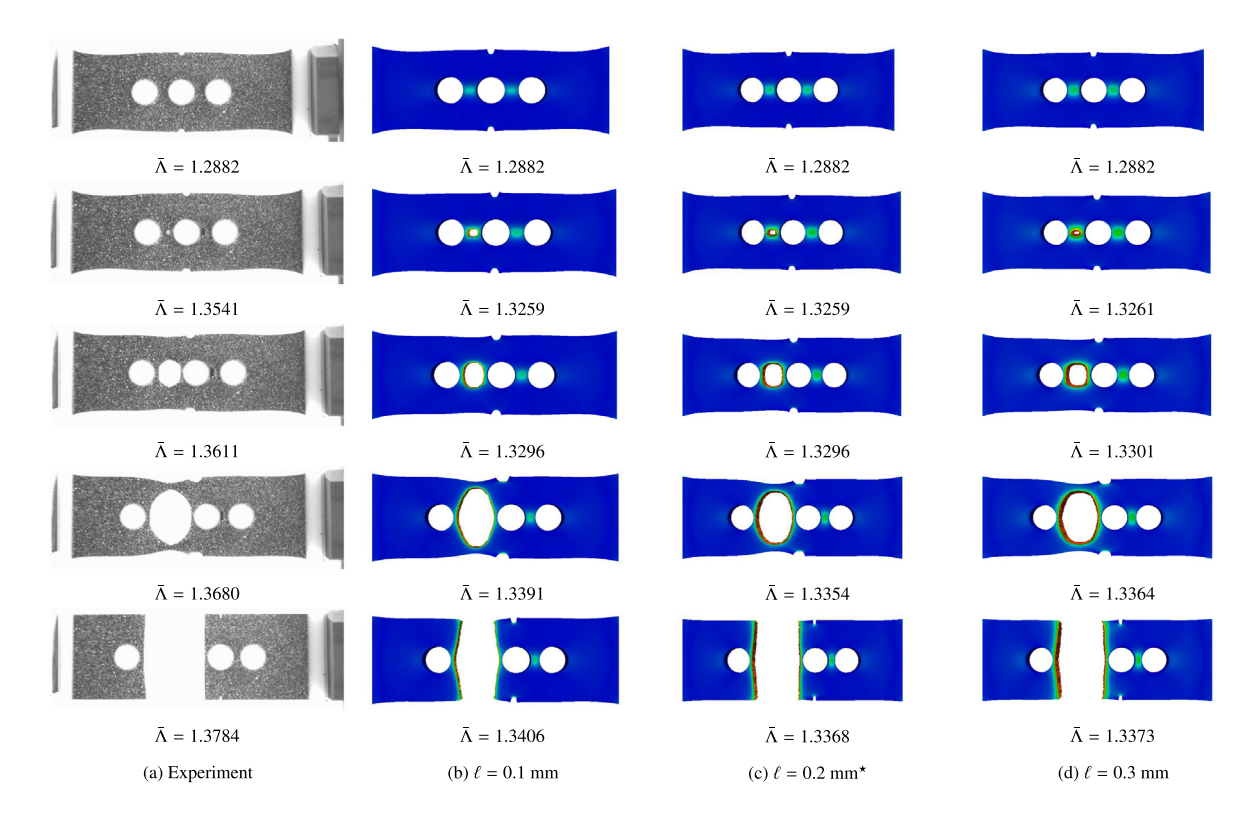


Fig. E.21. For studying the effect of length scale parameter ℓ , comparison of the crack paths at different global stretch values $\bar{\Lambda}$ for the N05D18 specimen obtained by (a) experiments, with those predicted by simulations using (b) $\ell=0.1$ mm with $\bar{\epsilon}_b^f=2.1$ MPa, (c) $\ell=0.2$ mm with $\bar{\epsilon}_b^f=1.6$ MPa and (d) $\ell=0.3$ mm with $\bar{\epsilon}_b^f=1.25$ MPa. The value $\ell=0.2$ mm is chosen in this study. Source: The experimental images are taken with permission from [85].

it can be concluded that the length scale does not play a vital role in the crack propagation path for the N20D30 specimen. The effects of the assumed notch radius and the smaller value of $\bar{\epsilon}_b^f$ chosen for the $\ell=0.3$ mm case are also studied on the crack propagation path for N05D30 specimen. As seen in Fig. E.23, the crack paths are not affected, and the length scale parameter can be concluded to be a major factor that influences the predicted fracture behavior of the N05D30 specimen.

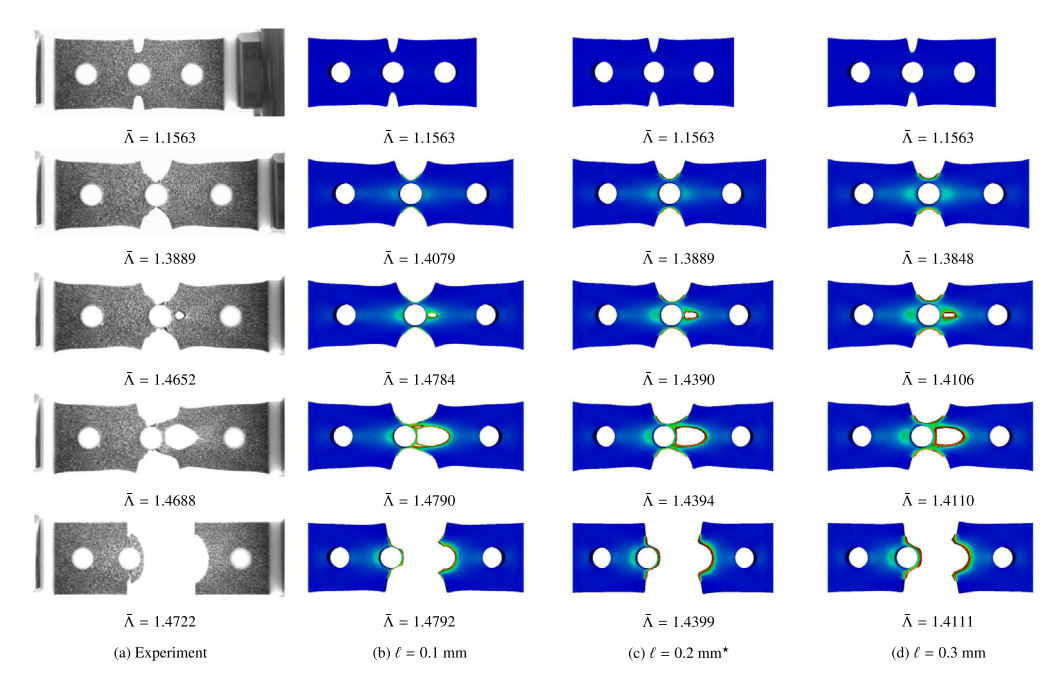


Fig. E.22. For studying the effect of length scale parameter ℓ , comparison of the crack paths at different global stretch values $\bar{\Lambda}$ for the N20D30 specimen obtained by (a) experiments, with those predicted by simulations using (b) $\ell=0.1$ mm with $\bar{\epsilon}_b^f=2.1$ MPa, (c) $\ell=0.2$ mm with $\bar{\epsilon}_b^f=1.6$ MPa and (d) $\ell=0.3$ mm with $\bar{\epsilon}_b^f=1.25$ MPa. The value $\ell=0.2$ mm is chosen in this study. Source: The experimental images are taken with permission from [85].

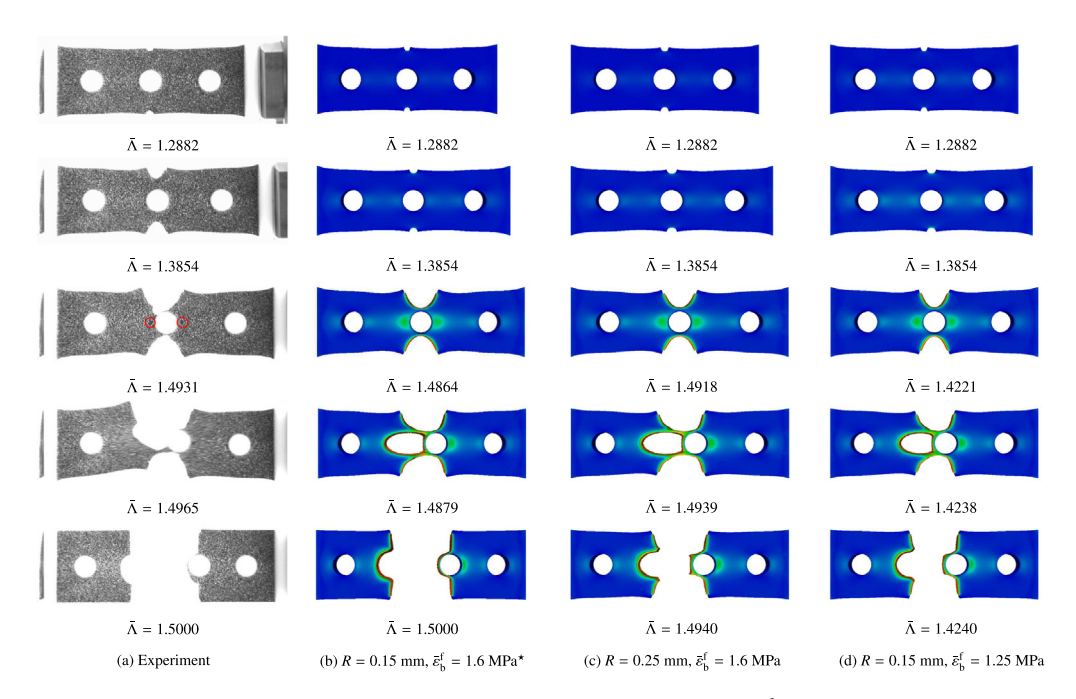


Fig. E.23. For studying the effect of notch radius R and the critical bond rupture energy $\tilde{\varepsilon}_b^f$, comparison of the crack paths at different global stretch values $\bar{\Lambda}$ for the N05D30 specimen obtained by (a) experiments, with those predicted by simulations using (b) R=0.15 mm, $\tilde{\varepsilon}_b^f=1.6$ MPa, (c) R=0.25 mm, $\tilde{\varepsilon}_b^f=1.6$ MPa and (d) R=0.15 mm, $\tilde{\varepsilon}_b^f=1.25$ MPa. The values R=0.15 mm, $\tilde{\varepsilon}_b^f=1.6$ MPa are chosen in this study.

Source: The experimental images are taken with permission from [85].

References

- [1] Y. Wang, C. Zhu, R. Pfattner, H. Yan, L. Jin, S. Chen, F. Molina-Lopez, F. Lissel, J. Liu, N.I. Rabiah, et al., A highly stretchable, transparent, and conductive polymer, Sci. Adv. 3 (3) (2017) e1602076.
- [2] J. Xu, S. Wang, G.-J.N. Wang, C. Zhu, S. Luo, L. Jin, X. Gu, S. Chen, V.R. Feig, J.W. To, et al., Highly stretchable polymer semiconductor films through the nanoconfinement effect, Science 355 (6320) (2017) 59–64.
- [3] C. Christianson, N.N. Goldberg, D.D. Deheyn, S. Cai, M.T. Tolley, Translucent soft robots driven by frameless fluid electrode dielectric elastomer actuators, Science Robotics 3 (17) (2018) eaat1893.
- [4] D. Zhalmuratova, H.-J. Chung, Reinforced gels and elastomers for biomedical and soft robotics applications, ACS Appl. Polym. Mater. 2 (3) (2020) 1073–1091.
- [5] Q. Chen, S. Liang, G.A. Thouas, Elastomeric biomaterials for tissue engineering, Prog. Polym. Sci. 38 (3-4) (2013) 584-671.
- [6] H. Ye, K. Zhang, D. Kai, Z. Li, X.J. Loh, Polyester elastomers for soft tissue engineering, Chem. Soc. Rev. 47 (12) (2018) 4545–4580.
- [7] L. Bernardi, R. Hopf, D. Sibilio, A. Ferrari, A.E. Ehret, E. Mazza, On the cyclic deformation behavior, fracture properties and cytotoxicity of silicone-based elastomers for biomedical applications, Polym. Test. 60 (2017) 117–123.
- [8] P.J. Loew, B. Peters, L.A. Beex, Rate-dependent phase-field damage modeling of rubber and its experimental parameter identification, J. Mech. Phys. Solids 127 (2019) 266–294.
- [9] S.J. Hashemi, A. Sadooghi, K. Rahmani, S. Nokbehrosta, Experimental determining the mechanical and stiffness properties of natural rubber FRT triangle elastic joint composite reinforcement by glass fibers and micro/nano particles, Polym. Test. 85 (2020) 106461.
- [10] V. Mittal, J.K. Kim, K. Pal, et al., Recent Advances in Elastomeric Nanocomposites, Vol. 9, Springer, 2011.
- [11] R. Rivlin, A.G. Thomas, Rupture of rubber. I. Characteristic energy for tearing, J. Polym. Sci. 10 (3) (1953) 291-318.
- [12] A.A. Griffith, VI. The phenomena of rupture and flow in solids, Philos. Trans. R. Soc. Lond. Ser. A 221 (582-593) (1921) 163-198.
- [13] R. Pidaparti, T. Yang, W. Soedel, Plane stress finite element prediction of mixed-mode rubber fracture and experimental verification, Int. J. Fract. 45 (3) (1990) 221–241.
- [14] N.A. Hocine, M.N. Abdelaziz, G. Mesmacque, Experimental and numerical investigation on single specimen methods of determination of J in rubber materials, Int. J. Fract. 94 (4) (1998) 321–338.
- [15] N.A. Hocine, M.N. Abdelaziz, A. Imad, Fracture problems of rubbers: J-integral estimation based upon η factors and an investigation on the strain energy density distribution as a local criterion, Int. J. Fract. 117 (1) (2002) 1–23.
- [16] N.A. Hocine, M.N. Abdelaziz, A new alternative method to evaluate the J-integral in the case of elastomers, Int. J. Fract. 124 (1) (2003) 79–92.
- [17] S. Kawabata, Fracture and mechanical behavior of rubber-like polymers under finite deformation in biaxial stress field, J. Macromol. Sci. B 8 (3-4) (1973) 605-630.
- [18] A. Hamdi, M.N. Abdelaziz, N.A. Hocine, P. Heuillet, N. Benseddiq, A fracture criterion of rubber-like materials under plane stress conditions, Polym. Test. 25 (8) (2006) 994–1005.
- [19] S. Mzabi, D. Berghezan, S. Roux, F. Hild, C. Creton, A critical local energy release rate criterion for fatigue fracture of elastomers, J. Polym. Sci. B 49 (21) (2011) 1518–1524.
- [20] F. Berto, A criterion based on the local strain energy density for the fracture assessment of cracked and V-notched components made of incompressible hyperelastic materials, Theor. Appl. Fract. Mech. 76 (2015) 17–26.
- [21] M.R. Ayatollahi, M. Heydari-Meybodi, M. Dehghany, F. Berto, A new criterion for rupture assessment of rubber-like materials under mode-I crack loading: the effective stretch criterion, Adv. Eng. Mater. 18 (8) (2016) 1364–1370.
- [22] P. Roy, D. Behera, E. Madenci, Peridynamic simulation of finite elastic deformation and rupture in polymers, Eng. Fract. Mech. 236 (2020) 107226.
- [23] G.A. Francfort, J.-J. Marigo, Revisiting brittle fracture as an energy minimization problem, J. Mech. Phys. Solids 46 (8) (1998) 1319–1342.
- [24] B. Bourdin, G.A. Francfort, J.-J. Marigo, Numerical experiments in revisited brittle fracture, J. Mech. Phys. Solids 48 (4) (2000) 797–826.
- [25] C. Miehe, L.-M. Schänzel, Phase field modeling of fracture in rubbery polymers. Part I: Finite elasticity coupled with brittle failure, J. Mech. Phys. Solids 65 (2014) 93–113.
- [26] A. Raina, C. Miehe, A phase-field model for fracture in biological tissues, Biomech. Model. Mechanobiol. 15 (3) (2016) 479-496.
- [27] O. Gültekin, H. Dal, G.A. Holzapfel, A phase-field approach to model fracture of arterial walls: theory and finite element analysis, Comput. Methods Appl. Mech. Engrg. 312 (2016) 542–566.
- [28] P. Zhang, X. Hu, T.Q. Bui, W. Yao, Phase field modeling of fracture in fiber reinforced composite laminate, Int. J. Mech. Sci. 161 (2019) 105008.
- [29] T.K. Mandal, V.P. Nguyen, J.-Y. Wu, A length scale insensitive anisotropic phase field fracture model for hyperelastic composites, Int. J. Mech. Sci. 188 (2020) 105941.
- [30] C. Miehe, M. Hofacker, L.-M. Schänzel, F. Aldakheel, Phase field modeling of fracture in multi-physics problems. Part II. Coupled brittle-to-ductile failure criteria and crack propagation in thermo-elastic-plastic solids, Comput. Methods Appl. Mech. Engrg. 294 (2015) 486–522.
- [31] M. Ambati, R. Kruse, L. De Lorenzis, A phase-field model for ductile fracture at finite strains and its experimental verification, Comput. Mech. 57 (1) (2016) 149–167.
- [32] S. Abrari Vajari, M. Neuner, P.K. Arunachala, A. Ziccarelli, G. Deierlein, C. Linder, A thermodynamically consistent finite strain phase field approach to ductile fracture considering multi-axial stress states, Comput. Methods Appl. Mech. Engrg. 400 (2022) 115467.
- [33] Y. Mao, L. Anand, A theory for fracture of polymeric gels, J. Mech. Phys. Solids 115 (2018) 30-53.

- [34] G. Zhang, T.F. Guo, Z. Zhou, S. Tang, X. Guo, A phase-field model for fracture in water-containing soft solids, Eng. Fract. Mech. 212 (2019) 180–196.
- [35] J. Wu, C. McAuliffe, H. Waisman, G. Deodatis, Stochastic analysis of polymer composites rupture at large deformations modeled by a phase field method, Comput. Methods Appl. Mech. Engrg. 312 (2016) 596–634.
- [36] A. Kumar, G.A. Francfort, O. Lopez-Pamies, Fracture and healing of elastomers: A phase-transition theory and numerical implementation, J. Mech. Phys. Solids 112 (2018) 523–551.
- [37] B. Yin, M. Kaliske, Fracture simulation of viscoelastic polymers by the phase-field method, Comput. Mech. 65 (2) (2020) 293-309.
- [38] F. Tian, J. Zeng, X. Tang, T. Xu, L. Li, A dynamic phase field model with no attenuation of wave speed for rapid fracture instability in hyperelastic materials, Int. J. Solids Struct. 202 (2020) 685–698.
- [39] M. Marulli, A. Valverde-González, A. Quintanas-Corominas, M. Paggi, J. Reinoso, A combined phase-field and cohesive zone model approach for crack propagation in layered structures made of nonlinear rubber-like materials, Comput. Methods Appl. Mech. Engrg. 395 (2022) 115007.
- [40] F. Peng, W. Huang, Y. Ma, Z.-Q. Zhang, N. Fu, Fourth-order phase field model with spectral decomposition for simulating fracture in hyperelastic material, Fatigue Fract. Eng. Mater. Struct. 44 (9) (2021) 2372–2388.
- [41] J.-Y. Ye, L.-W. Zhang, J. Reddy, Large strained fracture of nearly incompressible hyperelastic materials: Enhanced assumed strain methods and energy decomposition, J. Mech. Phys. Solids 139 (2020) 103939.
- [42] F. Tian, J. Zeng, M. Zhang, L. Li, Mixed displacement–pressure-phase field framework for finite strain fracture of nearly incompressible hyperelastic materials, Comput. Methods Appl. Mech. Engrg. 394 (2022) 114933.
- [43] I. Ang, N. Bouklas, B. Li, Stabilized formulation for phase-field fracture in nearly incompressible hyperelasticity, Internat. J. Numer. Methods Engrg. (2022).
- [44] F. Tian, M. Zhang, J. Zeng, B. Li, L. Li, Adaptive stabilized mixed formulation for phase field fracture modeling of nearly incompressible finite elasticity, Int. J. Mech. Sci. (2022) 107753.
- [45] C. Chen, Z. Wang, Z. Suo, Flaw sensitivity of highly stretchable materials, Extreme Mech. Lett. 10 (2017) 50-57.
- [46] P.K. Arunachala, R. Rastak, C. Linder, Energy based fracture initiation criterion for strain-crystallizing rubber-like materials with pre-existing cracks, J. Mech. Phys. Solids 157 (2021) 104617.
- [47] H.M. James, E. Guth, Theory of the elastic properties of rubber, J. Chem. Phys. 11 (10) (1943) 455-481.
- [48] M.C. Wang, E. Guth, Statistical theory of networks of non-Gaussian flexible chains, J. Chem. Phys. 20 (7) (1952) 1144–1157.
- [49] E.M. Arruda, M.C. Boyce, A three-dimensional constitutive model for the large stretch behavior of rubber elastic materials, J. Mech. Phys. Solids 41 (1993) 389–412.
- [50] C. Miehe, S. Göktepe, F. Lulei, A micro-macro approach to rubber-like materials—part I: the non-affine micro-sphere model of rubber elasticity, J. Mech. Phys. Solids 52 (11) (2004) 2617–2660.
- [51] H. Dal, M. Kaliske, A micro-continuum-mechanical material model for failure of rubber-like materials: Application to ageing-induced fracturing, J. Mech. Phys. Solids 57 (8) (2009) 1340–1356.
- [52] H. Dal, O. Gültekin, K. Açıkgöz, An extended eight-chain model for hyperelastic and finite viscoelastic response of rubberlike materials: Theory, experiments and numerical aspects, J. Mech. Phys. Solids 145 (2020) 104159.
- [53] C. Miehe, S. Göktepe, A micro-macro approach to rubber-like materials. Part II: The micro-sphere model of finite rubber viscoelasticity, J. Mech. Phys. Solids 53 (10) (2005) 2231–2258.
- [54] C. Linder, M. Tkachuk, C. Miehe, A micromechanically motivated diffusion-based transient network model and its incorporation into finite rubber viscoelasticity, J. Mech. Phys. Solids 59 (10) (2011) 2134–2156.
- [55] S. Göktepe, C. Miehe, A micro-macro approach to rubber-like materials. Part III: The micro-sphere model of anisotropic Mullins-type damage, J. Mech. Phys. Solids 53 (10) (2005) 2259–2283.
- [56] S.J. Mistry, S. Govindjee, A micro-mechanically based continuum model for strain-induced crystallization in natural rubber, Int. J. Solids Struct. 51 (2) (2014) 530–539.
- [57] G. Lake, A. Thomas, The strength of highly elastic materials, Proc. R. Soc. Lond. Ser. A Math. Phys. Sci. 300 (1460) (1967) 108-119.
- [58] Y. Mao, B. Talamini, L. Anand, Rupture of polymers by chain scission, Extreme Mech. Lett. 13 (2017) 17-24.
- [59] B. Talamini, Y. Mao, L. Anand, Progressive damage and rupture in polymers, J. Mech. Phys. Solids 111 (2018) 434-457.
- [60] B. Li, N. Bouklas, A variational phase-field model for brittle fracture in polydisperse elastomer networks, Int. J. Solids Struct. 182 (2020) 193–204.
- [61] J. Mulderrig, B. Li, N. Bouklas, Affine and non-affine microsphere models for chain scission in polydisperse elastomer networks, Mech. Mater. 160 (2021) 103857.
- [62] M. Tkachuk, C. Linder, The maximal advance path constraint for the homogenization of materials with random network microstructure, Phil. Mag. 92 (22) (2012) 2779–2808.
- [63] S. Swamynathan, S. Jobst, D. Kienle, M.-A. Keip, Phase-field modeling of fracture in strain-hardening elastomers: Variational formulation, multiaxial experiments and validation, Eng. Fract. Mech. 265 (2022) 108303.
- [64] A.N. Gent, A new constitutive relation for rubber, Rubber Chem. Technol. 69 (1) (1996) 59-61.
- [65] Q. Guo, F. Zaïri, A micromechanics-based model for deformation-induced damage and failure in elastomeric media, Int. J. Plast. 140 (2021) 102976.
- [66] B. Persson, E. Brener, Crack propagation in viscoelastic solids, Phys. Rev. E 71 (3) (2005) 036123.
- [67] M. Kroon, Steady-state crack growth in rubber-like solids, Int. J. Fract. 169 (1) (2011) 49-60.
- [68] H. Mueller, W. Knauss, The fracture energy and some mechanical properties of a polyurethane elastomer, Trans. Soc. Rheol. 15 (2) (1971) 217–233.
- [69] W. Kuhn, F. Grün, Beziehungen zwischen elastischen konstanten und dehnungsdoppelbrechung hochelastischer stoffe, Kolloid-Z. 101 (3) (1942) 248–271.

- [70] L.R.G. Treloar, The Physics of Rubber Elasticity, Oxford University Press, USA, 1975.
- [71] R. Rastak, C. Linder, A non-affine micro-macro approach to strain-crystallizing rubber-like materials, J. Mech. Phys. Solids 111 (2018) 67–99
- [72] B.D. Coleman, W. Noll, The thermodynamics of elastic materials with heat conduction and viscosity, Arch. Ration. Mech. Anal. 13 (1963) 167–178.
- [73] P. Flory, Thermodynamic relations for high elastic materials, Trans. Faraday Soc. 57 (1961) 829–838.
- [74] P. Wu, E. Van Der Giessen, On improved network models for rubber elasticity and their applications to orientation hardening in glassy polymers, J. Mech. Phys. Solids 41 (3) (1993) 427–456.
- [75] M. Kroon, A constitutive model for strain-crystallising rubber-like materials, Mech. Mater. 42 (9) (2010) 873-885.
- [76] M.C. Boyce, E.M. Arruda, Constitutive models of rubber elasticity: a review, Rubber Chem. Technol. 73 (3) (2000) 504-523.
- [77] J. Schröder, P. Neff, Invariant formulation of hyperelastic transverse isotropy based on polyconvex free energy functions, Int. J. Solids Struct. 40 (2) (2003) 401–445.
- [78] M. Neuner, R.A. Regueiro, C. Linder, A unified finite strain gradient-enhanced micropolar continuum approach for modeling quasi-brittle failure of cohesive-frictional materials, Int. J. Solids Struct. 254 (2022) 111841.
- [79] A. Thomas, Rupture of rubber. II. The strain concentration at an incision, J. Polym. Sci. 18 (88) (1955) 177–188.
- [80] C. Miehe, M. Hofacker, F. Welschinger, A phase field model for rate-independent crack propagation: Robust algorithmic implementation based on operator splits, Comput. Methods Appl. Mech. Engrg. 199 (45–48) (2010) 2765–2778.
- [81] P. Bažant, B. Oh, Efficient numerical integration on the surface of a sphere, ZAMM-J. Appl. Math. Mech./Z. Angew. Math. Mech. 66 (1) (1986) 37–49.
- [82] C. Miehe, F. Welschinger, M. Hofacker, Thermodynamically consistent phase-field models of fracture: Variational principles and multi-field FE implementations, Internat. J. Numer. Methods Engrg. 83 (10) (2010) 1273–1311.
- [83] C.J. Permann, D.R. Gaston, D. Andrš, R.W. Carlsen, F. Kong, A.D. Lindsay, J.M. Miller, J.W. Peterson, A.E. Slaughter, R.H. Stogner, R.C. Martineau, MOOSE: Enabling massively parallel multiphysics simulation, SoftwareX 11 (2020) 100430, http://dx.doi.org/10.1016/j.softx.2020.100430, URL: http://www.sciencedirect.com/science/article/pii/S2352711019302973.
- [84] R. Poya, A.J. Gil, R. Ortigosa, A high performance data parallel tensor contraction framework: Application to coupled electro-mechanics, Comput. Phys. Comm. (2017) http://dx.doi.org/10.1016/j.cpc.2017.02.016, URL: http://www.sciencedirect.com/science/article/pii/S0010465517300681.
- [85] J. Russ, V. Slesarenko, S. Rudykh, H. Waisman, Rupture of 3D-printed hyperelastic composites: Experiments and phase field fracture modeling, J. Mech. Phys. Solids 140 (2020) 103941.
- [86] V. Slesarenko, S. Rudykh, Towards mechanical characterization of soft digital materials for multimaterial 3D-printing, Internat. J. Engrg. Sci. 123 (2018) 62–72.
- [87] K. Mang, A. Fehse, N.H. Kröger, T. Wick, A mixed phase-field fracture model for crack propagation in punctured epdm strips, Theor. Appl. Fract. Mech. 115 (2021) 103076.
- [88] M.J. Borden, T.J. Hughes, C.M. Landis, C.V. Verhoosel, A higher-order phase-field model for brittle fracture: Formulation and analysis within the isogeometric analysis framework, Comput. Methods Appl. Mech. Engrg. 273 (2014) 100–118.
- [89] M.E. Gurtin, Generalized Ginzburg-Landau and Cahn-Hilliard equations based on a microforce balance, Physica D 92 (3–4) (1996) 178–192.
- [90] H. Stumpf, K. Hackl, Micromechanical concept for the analysis of damage evolution in thermo-viscoelastic and quasi-brittle materials, Int. J. Solids Struct. 40 (6) (2003) 1567–1584.
- [91] L. Anand, A constitutive model for compressible elastomeric solids, Comput. Mech. 18 (5) (1996) 339-355.